Effects of Axisymmetric Square-Wave Excitation on Transverse Jet Structure and Mixing

Takeshi Shoji,* Andrea Besnard,† Elijah W. Harris,† Robert T. M'Closkey,‡ and Ann R. Karagozian§
University of California, Los Angeles, Los Angeles, California 90095

DOI: 10.2514/1.J057982

The influence of temporal square-wave excitation on structural and mixing characteristics of an equidensity, gaseous jet in crossflow (JICF) was explored in the present study. As in separate unforced and sinusoidally excited JICF experiments, acetone planar laser-induced fluorescence imaging enabled this detailed quantification for the JICF for mean jet-to-crossflow momentum flux ratios J ranging from $J = 41$ (with a convective unstable upstream shear layer, or USL, in the absence of forcing) to $J = 5$ (with a globally unstable USL). Such square-wave excitation of the jet fluid required adaptive feedforward control, not only to create more accurate temporal square waveforms but to enable more accurate comparison among alternative forcing conditions. Square-wave excitation of the JICF demonstrated a significant influence on the naturally globally unstable JICF, where specific nondimensional stroke ratios within J-dependent ranges could produce deeply penetrating, periodic vortices with improved jet penetration and spread. Enhanced jet penetration did not always correlate with better molecular mixing, however; there was a stronger correlation of improved mixing at higher J values with creation of a more symmetric jet cross section via square-wave excitation, especially one with a clear counter-rotating vortex pair structure.

Nomenclature

C	=	local jet concentration at a pixel element
$\bar{C}$	=	mean concentration of jet fluid over all instantaneous images
C_o	=	mean concentration of jet fluid in the potential core region
C_m	=	local maximum mean concentration of jet fluid
D	=	jet nozzle diameter, m
f_f	=	forcing frequency, Hz
f_o	=	natural (fundamental) frequency of jet's upstream shear layer, Hz
J	=	jet-to-crossflow momentum flux ratio; $\rho_j U_j^2/\rho_\infty U_\infty^2$
L/D	=	stroke ratio
R	=	jet-to-crossflow velocity ratio; U_j/U_∞
Re_j	=	jet Reynolds number; $\rho_j U_j D/\mu_j$
S	=	jet-to-crossflow density ratio; ρ_j/ρ_∞
Sc_j	=	jet Schmidt number; $\nu_j/\hat{D}_{j\to\infty}$
s	=	upstream shear-layer trajectory coordinate, m
s_c	=	jet fluid concentration centerline trajectory in question, m
$s_{c,\text{unforced}}$	=	unforced jet fluid concentration centerline trajectory, m
T	=	period, s
U_c	=	center-plane-based unmixedness, %
U_j, U_∞	=	mean jet and freestream crossflow velocities, m/s
U_{yz}	=	cross-section-based unmixedness, %
u_j	=	temporally evolving jet velocity at center of jet exit plane, m/s
$\bar{u}_j$	=	jet velocity at the center of the jet exit, averaged over time τ, m/s
$u'_{j,\text{rms}}$	=	root mean square of the jet velocity perturbation relative to U_j, m/s
x, y, z	=	downstream, spanwise, and axial coordinates measured from jet orifice, m
z_p	=	jet penetration, m
Δu_j	=	peak-to-peak velocity amplitude of square-wave pulse at center of jet exit, m/s
τ	=	temporal pulse width, s

I. Introduction

TRANSVERSE jets or perpendicularly injected jets in crossflow (JICFs) are relevant to a variety of aerospace propulsion and energy generation systems [1,2], involving both airbreathing and rocket applications. As indicated in Fig. 1, the flush injection of a round jet with mean velocity U_j into a crossflow with freestream velocity U_∞ generates a number of complex vortical structures that contribute to specific structural and mixing features of the JICF [3–8]. These vortical structures include upstream shear layer (USL) vortices [5,6,9,10], horseshoe vortices that form in the plane of the jet injection wall [11], upright wake vortices that draw wall boundary-layer fluid into the jet itself [4], and the well-known counter-rotating vortex pair (CVP), which has long been understood to be the dominant feature of the transverse jet's cross section [3,5–7,12]. In the figure, the trajectory of the transverse jet's upstream shear layer (USL) is parameterized by the coordinate s, whereas the trajectory of the transverse jet's concentration-based centerline is characterized by the coordinate s_c determined via a power-law fit [8]. Structural and other features of the JICF have been characterized over the years for a range of nondimensional parameters, including the jet-to-crossflow density ratio $S = \rho_j/\rho_\infty$, velocity ratio $R = U_j/U_\infty$, and momentum flux ratio $J = \rho_j U_j^2/\rho_\infty U_\infty^2 = SR^2$, in addition to the jet Reynolds number $Re_j = \rho_j U_j D/\mu_j$, based on jet diameter D and jet dynamic viscosity μ_j. The Schmidt number of the jet represents the ratio of viscous to diffusion effects, $Sc_j = \nu_j/\hat{D}_{j\to\infty}$, where $\hat{D}_{j\to\infty}$ is the binary mass diffusivity for the jet fluid into the crossflow fluid.

Extensive recent experimental studies of the gaseous, nonreactive JICF have focused on USL stability as well as jet structural characteristics for a range of flow conditions in the absence of external forcing [7,13–15]. Additional studies quantify molecular mixing characteristics [8] and strain/scalar dissipation rate fields [16], again in the absence of any significant external jet excitation. Early experiments on the gaseous JICF [13,14] document for the first

Received 4 October 2018; revision received 21 December 2018; accepted for publication 24 December 2018; published online 31 January 2019.

*Postdoctoral Scholar, Department of Mechanical and Aerospace Engineering; currently Associate Administrator, Aeronautical Technology Directorate Propulsion Research Unit, Japan Aerospace Exploration Agency (JAXA), Tokyo 182, Japan.

†Graduate Student Researcher, Department of Mechanical and Aerospace Engineering.

‡Professor, Department of Mechanical and Aerospace Engineering.

§Professor, Department of Mechanical and Aerospace Engineering; ark@seas.ucla.edu. Fellow AIAA.

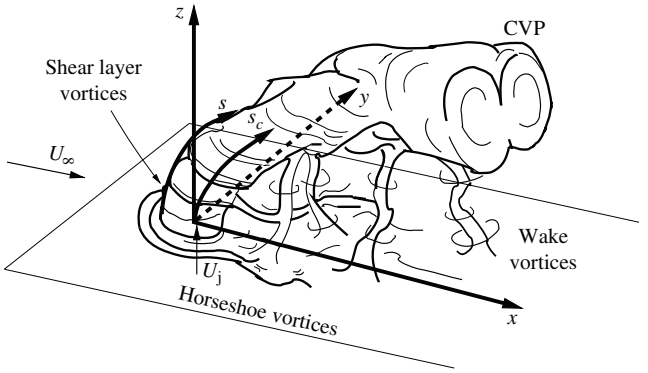

Fig. 1 Schematic of the JICF and relevant vortical structures. (x; y; z) represent jet coordinates, s represents the USL trajectory coordinate, and s_c represents the jet concentration-based centerline coordinate.

time a transition in the jet's upstream shear layer, from local convective instability at higher values of J or R, with relatively weak and broadband spectral peaks that evolve and grow spatially along the USL, to absolute instability at lower J or R values, with strong, pure tone spectral peaks that are rapidly initiated and dominate the flowfield, as observed for global instability in other nonparallel flows [17]. This USL transition is observed as the jet Reynolds number is fixed while crossflow velocity is increased, so that J or R is reduced. For example, for the equidensity ($S = 1$) flush nozzle-injected JICF for Reynolds numbers 1900–3000, the transition from convectively unstable to globally unstable behavior occurs near or below $R_{cr} \approx 3.1$ or $J_{cr} \approx 10$ for a pure nitrogen jet injected into a crossflow of air [13,14]. USL instabilities for the low-density jet in crossflow, explored via hot-wire anemometry by Getsinger et al. [15] and using jet mixtures of helium and nitrogen injected into air ($0.14 \leq S \leq 1.00$), show that the transition in the USL occurs for either a momentum flux ratio $J \lesssim 10$ or for density ratio $S \lesssim 0.40$. These critical values are altered somewhat for the JICF with the same jet and crossflow fluids but injected via an elevated nozzle into crossflow [7,13]. For the flush nozzle-injected, equidensity JICF, direct numerical simulations (DNS) by Iyer and Mahesh [18] predict the same upstream shear-layer spectral characteristics, both qualitatively and quantitatively, as in experimental studies using the same nozzle shape and jet and crossflow conditions as in experiments [13]. The correspondence applies to both convectively and globally unstable USL conditions (at $R = 4$ and 2, respectively).

Laser diagnostics can be used for the quantitative study of JICF structural and mixing characteristics. Acetone planar laser-induced fluorescence (PLIF) imaging in both the center-plane (x–z plane at $y = 0$) and cross-sectional planes (y–z planes at variable x values) enable an understanding of differences in jet structure based on different USL stability characteristics [7]; this study explores $2 \leq J \leq 41$, with additional data for various Reynolds numbers ($1000 \leq Re_j \leq 6500$). Among the more notable observations is the rather strongly asymmetric mean jet cross section at $J \geq 20$ for the flush nozzle, with a distorted and asymmetric CVP-like structure, whereas for the absolutely or globally unstable JICF, strong USL instabilities result in a symmetric mean cross-sectional CVP structure. Follow-on studies Gevorkyan et al. [8] use acetone PLIF to quantify mixing metrics for the equidensity and low-density transverse jet, for both convectively and absolutely/globally unstable USL conditions. It is found that jets with a globally unstable upstream shear layer and symmetric cross-sectional CVP tend to achieve greater molecular mixing than do jets at larger J values with less symmetric CVP structures and weaker convectively unstable upstream shear-layer instabilities.

Typical molecular mixing metrics are based on mean as well as instantaneous jet concentration images in both center-plane and cross-sectional views of the JICF. The unmixedness [19], which is also used in the present study as a mixing metric, expresses the variance of the scalar concentration field relative to the mean concentration value within an interrogation area (i.e., the second moment of the scalar concentration). For the JICF, unmixedness in a cross-sectional interrogation area in the y–z plane with dimensions $L_y \times L_z$, for example, is defined as follows:

$$U = \frac{1}{L_y L_z} \iint \frac{(C/C_o - \bar{C}/C_o)^2}{(\bar{C}/C_o)(1 - \bar{C}/C_o)} \, \mathrm{d}y \, \mathrm{d}z \tag{1}$$

where C/C_o represents the local instantaneous jet fluid concentration within a pixel element at (y, z), scaled by the concentration of pure jet fluid (C_o) within the potential core, and $\bar{C}/C_o$ represents the spatially averaged scaled concentration over the entire interrogation area at a given time. A lower unmixedness corresponds to better local molecular mixing in a flowfield, whereas larger values represent poorer mixing. Methods for calculating unmixedness using Eq. (1) in the present study are outlined later; more extensive details may be found in prior papers [8].

Temporal excitation of the jet fluid, with either sinusoidal or square waveforms, is known to alter the structural characteristics of the JICF, in particular its degree of penetration into the crossflow and its spatial spread, depending on flow and forcing conditions [20–26]. For example, for the liquid jet in liquid crossflow, Johari et al. [20] show that, for the fully modulated JICF with square-wave excitation at frequency f_f, a relatively small temporal pulse width τ (or duty cycle $\alpha \equiv f_f \tau$) can increase jet penetration as well as improve mixing via centerline decay enhancement. Other studies suggest significant improvements in jet penetration with square-wave excitation via periodically generated vortical structures [21], although sinusoidal excitation is observed to have a greater effect on the JICF primarily for higher velocity ratios [23]. In the presence of a chemical reaction between jet and crossflow fluid, the visible "flame length" can provide evidence of molecular mixing of species as a global metric [20,21,25], where a shorter flame length suggests improved mixing when viewed from the center plane (x–z plane).

Earlier University of California, Los Angeles (UCLA) based experiments document the effects of both sinusoidal and square-wave excitation of the JICF [22,24,26]. Smoke visualization enables quantification of jet penetration and spread for a rather wide range of velocity ratios ($1.15 \leq R \leq 10$), where smoke is seeded into the nitrogen jet in a crossflow of air. Davitian et al. [26] observe that the convectively unstable jet for $R > 3.1$ is strongly affected by even low-amplitude sine-wave forcing, with an increase in both penetration and spread during such excitation. But absolutely unstable jets with $R \leq 3$ are hardly affected at all by even high-amplitude sinusoidal forcing. To have an impact on the absolutely unstable JICF penetration and spread, Davitian et al. [26] determine that axisymmetric square-wave excitation, with a prescribed temporal pulse width $\boldsymbol{\tau}$ related to optimal vortex ring formation [27], is best able to create periodic, deeply penetrating vortical structures and thus to increase average jet penetration and spread. The ability to create fairly precise temporal square-wave (or other non-sine-wave) excitation for an absolutely unstable flow requires carefully tuned feedforward and/or feedback control [22,24,26], as will be discussed later.

Optimal vortex ring formation [27] is often expressed in terms of a nondimensional stroke ratio L/D, which characterizes the short temporal pulse during which fluid is introduced into a flowfield and potentially forms a vortex ring. For the JICF, one can relate L/D to the temporal pulse width τ of square-wave excitation measured at the jet exit. For example, Johari [25] relates L/D to τ for a fully modulated jet in which the time-varying local velocity at the jet exit periodically reaches zero. In this case, the stroke ratio reduces to the following relation:

$$\left(\frac{L}{D}\right)_{\mathrm{FM}} \cong \frac{\overline{u_j}\tau}{D} \tag{2}$$

$\overline{u_j}$ is the time- and area-averaged vertical velocity at the jet exit during the pulse. For various R or J values, the critical stroke ratio L/D at which distinct vortex rings form for transverse jet asymptotically is often around 4, corresponding to the "universal time scale" for vortex ring formation [27]. For the controlled JICF experiments in prior

UCLA studies [22,24,26], however, partially modulated square waveforms required a different approximation to the stroke ratio. For example, Shapiro et al. [24] estimate the peak-to-peak velocity amplitude of a square-wave pulse Δu_j as measured at the center of the jet exit and then approximate the stroke ratio as

$$\left(\frac{L}{D}\right)_{\mathrm{PP}} \cong \frac{\Delta u_j \tau}{D} \tag{3}$$

to effectively account for only fluid pulsation in creating pulses of vorticity. Nevertheless, optimal JICF vortex ring penetration and spread are generally found to correspond to estimated stroke ratios of order 4 [24,26], although in some lower-velocity ratio cases, optimal penetration is seen to occur at stroke ratios that were smaller than 4. A separate computational study of the partially modulated JICF with prescribed square-wave forcing at the jet exit plane conducted by Sau and Mahesh [28] indicates that the optimal stroke ratio L/D for creation of deeply penetrating vortical structures is reduced as J decreases, resulting from a structural transition from creation of distinct successive vortex rings to a vortex ring with a trailing column connected to subsequent structures. A relationship between stroke ratio L/D and the velocity ratio associated with a vortex ring distorted by the crossflow (studied in [29] and described in terms of a ring velocity ratio $r_{\mathrm{ring}} \equiv \Delta u_j / U_\infty$) is used to quantify these differences in vortex penetration.

The relevance of increased JICF penetration and spread arising from various types of jet excitation [24,26] to actual improvements in the molecular mixing of the jet with surrounding fluid has not been studied to any significant degree. This is one of the goals of the present study, which focuses on square-wave excitation of the jet for a range of flow and excitation conditions. A separate study involving sinusoidally excited JICF experiments [30] explores the effect of such excitation on jet molecular mixing via the unmixedness parameter described in Eq. (1), as well as using more traditional metrics such as jet penetration and spread. One focus in this separate study is on the effect of "lock in" of the upstream shear layer to the external sinusoidal excitation frequency f_f. Earlier studies demonstrate that the JICF can exhibit lock-in behavior [14,15], typical of a self-excited dynamical oscillator or absolutely/globally unstable flow [31], when f_f is applied at either a moderate amplitude close to the naturally occurring USL frequency f_o or when very high-amplitude forcing is applied at a frequency f_f that is further from f_o. In either instance, the excitation influences the shear layer's spectral character, both under globally unstable USL conditions (i.e., low J values) and for convectively unstable USL conditions (larger J values), explored in detail in [30]. With sinusoidal excitation, these studies demonstrate improved molecular mixing for the convectively unstable JICF, especially when the USL is locked in to the forcing frequency; this also causes the jet cross section to become more symmetric. For a globally unstable JICF, only sinusoidal forcing corresponding to clear lock-in conditions, close to the fundamental shear-layer frequency and/or at very high amplitudes, affects jet structure, with only moderate improvements in molecular mixing.

The impact of square-wave excitation of the jet in crossflow on actual molecular mixing, beyond alterations in jet structure, is the focus of the present experiments. These studies focus on the equidensity ($S = 1$), flush nozzle-injected JICF studied via acetone PLIF, imaged in both center-plane (x–z) and cross-sectional (y–z) planes to examine the relationships among jet structure, penetration, spread, and molecular mixing for various excitation conditions. To study conditions in which the unforced transverse jet has both convectively unstable and absolutely/globally unstable upstream shear layers, we examine several alternative values of the momentum flux ratio J ($J = 41$, 12, and 5) while fixing $Re_j = 1900$.

II. Experimental Configuration

A. Jet in Crossflow Wind Tunnel and Experimental Diagnostics

A low-speed wind tunnel was used to explore axisymmetrically forced JICF characteristics. A schematic of the wind tunnel and associated diagnostics is shown in Fig. 2. Air (creating the crosswind) entered the tunnel via a centrifugal blower (Baldor M3546-T) with flexible ducting to minimize mechanical vibration, temperature, and other effects on tunnel flow. The air then entered the test section through a 9:1 area ratio contraction section with honeycomb and screens [32], flowing in the positive x direction. The maximum achievable crossflow velocity in the test section was approximately 7 m/s, with a maximum turbulence intensity less than 1.5% in the freestream. A primary test section, fitted flush with the contraction section, was $30 \times 12 \times 12$ cm. A quartz window fitted onto the top of the test section provided laser sheet access to the jet flowfield, while a Plexiglas window was fitted into the side of the test section to enable optical access in the center plane for the camera. A black panel with a cutout could replace the side Plexiglas window for hot-wire anemometry access to the jet. A second tunnel section, not shown in Fig. 2, was followed by a wood cubic chamber ($30 \times 30 \times 30$ cm), allowing optical access from the downstream end of the tunnel

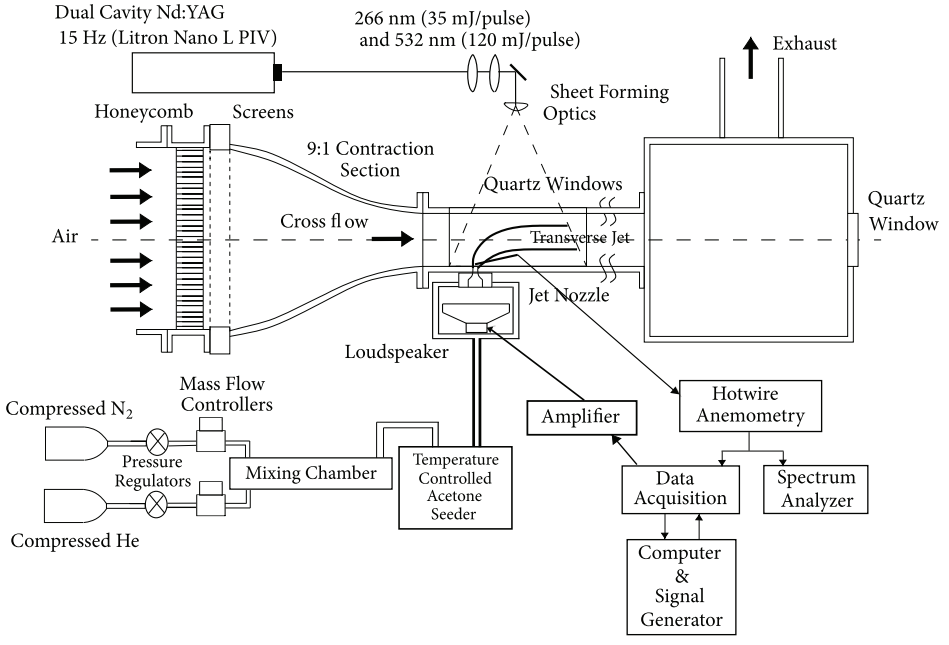

Fig. 2 Variable-density transverse jet wind tunnel, with associated data acquisition and optical diagnostic apparatus. One additional tunnel section, of identical dimensions, was situated downstream of the test section shown.

through a 90×90 mm quartz window for cross-sectional imaging in the y–z plane. The chamber exhausted the gases via a flexible tube mounted on the top into the ventilation system of the lab.

The transverse jet injection system consisted of a nozzle with a fifth-order polynomial shape (exit diameter $D = 4.04$ mm), with the exit plane flush with respect to the tunnel floor and with the nozzle mounted at a location 10 cm downstream of the end of the tunnel contraction. The nozzle's fifth-order polynomial shape created a top-hat-like velocity profile at the exit plane in the absence of crossflow, with a fairly thin jet boundary layer [13,16]. In the present studies, the jet fluid was composed of a mixture of He, N_2, and acetone vapor, with the latter used for laser diagnostics. Mass flow controllers (Tylan Model FC-260) were used to vary the He and N_2 mass flow rates; the gases were mixed in a chamber downstream of the flow controllers to passively remove nonuniformities, after which the mixture flowed into a temperature-controlled acetone seeder. The seeded mixture then entered four symmetrically center-oriented injectors beneath the injection system. Altering the mole fractions of acetone, helium and nitrogen enabled one to match the densities of jet fluid and crossflow (or for low-density JICF experiments, to achieve the desired density ratio S). The absolute viscosity of the jet mixture (μ_j) was determined from the mole fractions of constituent gases, including acetone, via the Reichenberg method [33]. In the present studies, the mole fractions of acetone, He, and N_2 in the jet fluid were 0.218, 0.234, and 0.548, respectively [30].

As noted previously, the jet Reynolds number and the density ratio were kept constant in the present experiments at $Re_j = 1900$ and $S = 1$, respectively, whereas the momentum flux ratio J was varied independently by altering the crossflow velocity U_∞. Crossflow conditions corresponded to a laminar wall boundary layer consistent with the Blasius profile, as documented in Getsinger et al. [7]; the crossflow boundary-layer thickness was at most 25% of the jet diameter [13]. In the present studies, jet-to-crossflow momentum flux ratios included those producing a convectively unstable USL in the absence of forcing ($J = 41$ and 12) and one producing a naturally globally unstable USL ($J = 5$).

Axisymmetric excitation for the JICF was applied from the bottom of the injection system, below a pipe connected to the nozzle, using an acoustic loudspeaker (RadioShack 40-1022B, 4 in. woofer) as shown in Fig. 2. The speaker was enclosed by a Plexiglas plenum housing attached to the bottom of the injection system. For sinusoidal excitation of the jet fluid, used for comparison with the present square-wave forcing studies, the temporal waveform was created by a function generator (BK Precision Model 4078) at a desired forcing frequency f_f and amplitude quantified via hot-wire measurement at the center of the exit plane of the jet. The initial signal was delivered to an amplifier (Adcom GFA-7300) with a constant gain of 30 for all excitation conditions; the amplified signal drove the loudspeaker to create the desired temporal jet waveform. To produce square-wave excitation of the jet fluid, a dSPACE 1104 DSP data acquisition (DAQ) board was used to generate superposition of 10 sinusoidal signals with the desired forcing frequency f_f and higher harmonics, up to $10f_f$, to create a square wave with the desired amplitude. Details on the adaptive feedforward control system required to create square-wave excitation are provided in Sec. II.B.

Constant-temperature anemometry (CTA) was used for these acetone-seeded JICF experiments, with and without external forcing, using a single-component, boundary-layer-type hot-wire probe (Dantec 55P15). The data taken by the hot wire were delivered first to a 90C10 CTA module in a Dantec StreamLine 90N10 frame and then to an ac/dc signal splitter with signal conditioning developed by Hendrickson [34]. The conditioned ac and dc signals were combined and analyzed by the DAQ board using ControlDesk software within Matlab's Simulink program at a sampling frequency of 20 kHz. The maximum forcing frequency (6000 Hz) resulted from the nonuniform frequency response of the actuation system, consisting of the amplifier, loudspeaker, hot wire, signal conditioner, and DAQ board. The uncertainties in the hot-wire measurements were largest at very low velocities; the largest uncertainties were of the order 1% for a velocity of 1 m/s, as documented in earlier studies [7].

The temporally varying jet velocity u_j was quantified via hot-wire anemometry at a location 0.2 jet diameters above the center of the jet exit plane. The rms of the jet velocity perturbation $u'_{j,\mathrm{rms}}$, relative to the mean jet velocity U_j, was used to quantify the amplitude of jet excitation and was defined as follows:

$$u'_{j,\mathrm{rms}} = \sqrt{\frac{1}{T}\int_{t_1}^{t_1+T} (u_j - U_j)^2 \, \mathrm{d}t} \tag{4}$$

where $T \equiv 1/f_f$ is the period of excitation. In the present studies, $u'_{j,\mathrm{rms}}$ was matched among different forcing conditions and waveforms, effectively matching the net periodic impulse introduced to the jet via excitation. The rms values explored here were in the range $1.0 \le u'_{j,\mathrm{rms}} \le 2.0$ m/s for each waveform identified, as compared with a mean jet velocity of $U_j \approx 6.5$ m/s. For square-wave excitation, matching $u'_{j,\mathrm{rms}}$ values required application of an adaptive feedforward controller, not only to create more accurate square waveforms but to enable accurate quantification of velocity-relevant parameters, as will be described in Sec. II.B. Square-wave forcing studies focused on $f_f = 100$ Hz, with a range of duty cycles or temporal pulse widths, to achieve the large number of higher harmonics required for a Fourier series to create a reasonable square waveform.

Acetone seeded in the jet fluid was used for planar laser-induced fluorescence (PLIF) imaging of the flowfield, enabling quantification of jet structural and mixing characteristics. Thus, to be able to quantify and match values of $u'_{j,\mathrm{rms}}$ for jet mixtures containing acetone, helium, and nitrogen, calibration of the hot wire operating in such mixtures was required. The present studies used a known velocity profile for a fully developed, flush pipe-injected jet in quiescent surroundings (as used in separate JICF experiments [8]) and applied this to calibrate the hot wire for a range of jet Reynolds numbers, $300 \le Re_j \le 2300$ [30]. $u'_{j,\mathrm{rms}}$ in the flush nozzle-injected JICF experiments was measured at a location 0.2 jet diameters above the center of the jet exit plane, corresponding to the potential core region of the jet for all flow conditions in this study, where there was little variation in local mole fraction of acetone. Hence, only a single calibration curve at this single mole fraction of acetone ($\psi = 0.218$) was sufficient to properly measure $u'_{j,\mathrm{rms}}$.

As noted previously, PLIF imaging of acetone vapor seeded in the jet was used to study jet structural and mixing characteristics, as done in prior nonforced JICF experiments [7,8,16] and in sinusoidally excited jet experiments [30]. Acetone is extensively used as a molecular tracer for PLIF [35–38], and the optical setup for these nonintrusive diagnostics is shown in Fig. 2. A dual-cavity Q-switched Nd:YAG laser (Litron Nano L PIV) was employed in these experiments with second and fourth harmonic generators. This enabled creation of concentric beams in the visible (at 532 nm, for separate particle image velocimetry experiments [7,16]) and ultraviolet (at 266 nm, for the present PLIF experiments). Each cavity was able to produce an 8 ns full width at half maximum pulse with 30 mJ output at 266 nm at the maximum repetition rate of 15 Hz, although the actual repetition rate used was 7.5 Hz. There was no phase locking of the imaging to the external excitation; hence, forcing frequency f_f had to be selected so as not to be divisible by the recording rate to avoid capturing images only at a single phase. The recording rate was confirmed not to affect JICF mixing characteristics when averaging data over 500 image realizations [30], which is what was used in these studies to achieve statistical convergence of image data.

In the present experiments, the light emitted by the laser passed through two 266 nm dichroic mirrors and a 3-mm-thick uncoated UV-grade fused silica window, two spherical lenses to enable focusing at a desired location, a turning mirror for a 90 deg viewing direction, an $f = -10$ mm cylindrical lens, and through the quartz window at the top of the test section, forming a divergent sheet oriented at the desired orientation within the test section. The dichroic mirrors diminished the green light energy and transmitted the 266 nm UV beam for acetone PLIF, and the UV fused silica window after the dichroic mirrors reflected approximately 7% of the 266 nm beam

energy to enable measurement of a portion of the laser energy using a pyroelectric energy detector. The monitored laser energy was eventually applied in PLIF image processing, in particular for background subtraction and laser absorption correction, as a scaling factor. To introduce the appropriate proportions of acetone and other gases into the jet fluid, two acetone seeder chambers were placed upstream of the nozzle injection system. The second acetone seeder's chamber pressure and temperature were continuously monitored via a pressure transducer (Omega PX409-015G5V) and a type T thermocouple to attain the appropriate vapor conditions.

For both center-plane and cross-sectional PLIF imaging, a 14-bit charge-coupled device camera (LaVision Imager proX) with 1600×1200 pixel resolution recorded the acetone-seeded JICF fluorescence intensity. Calibration of the camera was performed with a two-plane calibration plate (LaVision Type 7), after which image coordinates could be transformed into the laboratory reference frame. Further image processing involved bias noise correction, flat-field correction, background subtraction, laser energy absorption correction, and two-pass image filtering. For center-plane images, the normalization of concentration values was performed using a mean concentration value in the potential core region of the jet for each instantaneous image. For calibration of concentration values in cross-sectional images, a normalized mean center-plane image was used, and average concentration data within a thin slice (7 pixels wide) at the specific x location allowed calibration of concentration data in the cross-sectional image at the same x location. The 266 nm laser sheet thickness, based on the $1/e^2$ criterion, was measured by the scanning knife-edge technique [39,40] to be approximately 400–900 μm within the optical field of view. The in-plane pixel size of center-plane PLIF images was 80 μm per pixel, whereas the pixel size ranged from 60 to 90 μm for cross-sectional PLIF images, depending on the x/D location. For the present diffusion-limited flowfield, a conservative estimate of the smallest required resolution is related to the strain-limited diffusion scale (λ_D), which is estimated to be 350 μm in the present study [16,38]. Hence, according to the Nyquist criterion, the required spatial resolution for PLIF imaging (175 μm) is easily met by both the in-plane and the cross-sectional spatial resolution. This gives greater confidence that the current optical configuration is able to characterize and quantify JICF molecular mixing. Further details on the optical diagnostics are provided in prior publications [8,16,30,41].

B. Square-Wave Excitation via Adaptive Feedforward Control

Among the main challenges in exploring the effects of square-wave forcing on the JICF was the creation of the square temporal waveform itself, typically measured at the jet exit plane. An inherently imperfect, nonflat frequency response of the actuation system (consisting of the amplifier, loudspeaker, flush nozzle, hot wire, signal conditioning), as well as nonlinear interactions among all subharmonic and harmonic disturbances, introduced challenges in creating a precise temporal square waveform at the jet exit [22,24,30]. In contrast, sinusoidal jet excitation can be reasonably achieved at the desired forcing frequency f_f and amplitude of excitation $u'_{j,\mathrm{rms}}$ by altering the gain settings in the actuation system. In both sinusoidal and square-wave forcing cases, the input to be manipulated was the amplifier input signal, and the output to be adjusted was the jet velocity as measured by the hot wire. Our group at UCLA developed several strategies for achieving temporal square-wave excitation. Early work employed a feedforward filter based on the causal inversion of a broadband model of the actuation system [22,24]. This approach was successful in creating well-defined pulses, but control over the inter-pulse behavior was challenging. Because periodic jet velocities were desired, though, a simpler approach was used in [26], whereby a truncated Fourier series of the desired periodic jet velocity was approximated by adjusting the magnitude and phase of the actuator input sinusoids specified at the same frequencies as truncated jet waveform. The magnitude and phase of the input sinusoids, however, were determined from the empirical frequency response of the jet actuation like the earlier publications, and because the empirical frequency response is based on estimating the "best" linear model in a least-squares sense, its application in determining the input sinusoids inevitably produced a jet velocity waveform that deviated from the desired waveform despite providing the sharp transitions in the pulses.

The next step in the evolution of the jet velocity shaping was to build a map, discussed in greater detail later for the present research, that links all input and output harmonics in the partial Fourier series representations of the periodic amplifier input and jet velocity. This approach has the advantage of explicitly estimating the effect of changes in a given input sinusoid on the corresponding output sinusoid and its neighboring harmonics. Thus, the nonlinearities present in the system are captured about the local operating point. The results in [42,43] showed how these maps can be identified and then used to produce a control law to adjust the input harmonics such that the output harmonics converge to the desired jet velocity waveform. The control was shown to be robust in the sense that the identified maps were determined about operating points that are not the desired operating point, yet the controller was able to drive the jet velocity to the desired waveform. Although this method proved quite effective for creating many jet velocity waveforms, its potential disadvantage was the amount of real-time computation required to implement the controller in addition to the complex controller design process itself.

The present study is based on these ideas but is less demanding in its real-time computational requirements and does not explicitly require the design of a controller. To create a temporal square waveform with a desired forcing frequency f_f (or period $T \equiv 1/f_f$), temporal pulse width τ (or duty cycle $\alpha \equiv \tau/T$), and amplitude $u'_{j,\mathrm{rms}}$, the amplifier input is a superposition of 10 sinusoidal components of a Fourier series (from f_f up to $10f_f$). For these experiments, $f_f = 100$ Hz, with higher harmonics up to 1000 Hz, beyond which the actuation system frequency response naturally began to roll off. Because the ability to control the jet velocity above 1000 Hz is diminished, this range covers the available bandwidth of the actuation system. The forcing frequency f_f was chosen to enable a clearer contrast with sine-wave forcing at the same forcing frequency, which may or may not have achieved lock-in, depending on forcing amplitude [30]. Note that the presence of acetone alters the fundamental frequency of the instability via small changes in the jet fluid viscosity [30]; therefore, this behavior must be included in characterization of the actuation system for each of the J values examined.

A description of the process for determining the amplitudes and phases of the 10 sinusoidal input components is now given. It is easier to work with amplitudes of the $\cos(kf_f t)$ and $\sin(kf_f t)$ functions at frequency kf_t, $k = 1, 2, \ldots, 10$, instead of the amplitude and phase of a single sinusoidal term; thus, the input signal is quantified by a 20-element real-valued vector denoted $\boldsymbol{a}$ (i.e., $\boldsymbol{a} \in \mathbb{R}^{20}$). Similarly, a 20-element vector denoted $\boldsymbol{d} \in \mathbb{R}^{20}$ also represents the periodic jet velocity corresponding to the input defined by $\boldsymbol{a}$. The underlying assumption in the present work as well as [42,43] is that $\boldsymbol{d}$ is related to $\boldsymbol{a}$ by a continuously differentiable function F. For a linear time-invariant system, F is well-defined and can be determined from the system's frequency response function; however, there is currently no formal proof of the existence of such a function for the nonlinear system representing the jet-in-crossflow. The main justification for F is due to the fact that conceptual framework it provides works well in practice for guiding the adjustment of the amplifier input to drive the jet velocity to the desired waveform. For a nominal periodic input $\boldsymbol{a}_0$ with corresponding jet velocity $\boldsymbol{d}_0$ [i.e., $\boldsymbol{d}_0 = F(\boldsymbol{a}_0)$], deviations in a neighborhood of this operating point can be approximated as $\boldsymbol{d}_0 + \delta_d \approx F(\boldsymbol{a}_0) + K(\boldsymbol{a}_0)\delta_a$, where δ_a and δ_d represent the deviations in the periodic input and output, respectively, and $K(\boldsymbol{a}_0) \in \mathbb{R}^{20\times 20}$ is the Jacobian of F. In practice, F is not explicit identified; however, $K(\boldsymbol{a}_0)$ is determined from experiments in which the elements of $\boldsymbol{a}_0$ are sequentially perturbed and the corresponding jet velocity perturbations δ_d are measured. Although this appears time consuming, the identification process can be automated and the Fourier coefficients can be simply determined from the discrete Fourier transform of the jet velocity measurements.

An initial operating point is required and is determined by using the desired jet velocity components, represented by $\bar{\boldsymbol{d}}$, and the

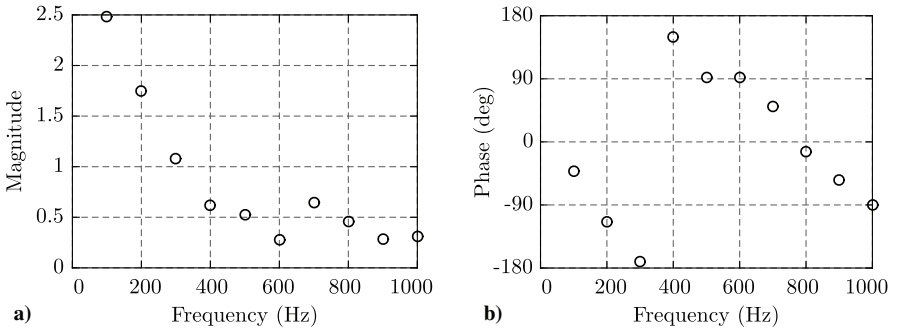

Fig. 3 Typical frequency response of the actuation system from 100 to 1000 Hz, with data for the acetone-seeded JICF with $J = 5$. Shown are: a) magnitude, and b) phase.

"frequency response" of the system. The target jet velocity in these experiments is periodic rectangular pulse with fundamental frequency f_f and duty cycle α, with the rms of the jet's vertical velocity perturbation given by $u'_{j,\mathrm{rms}}$. The frequency response is determined simply correlating the jet velocity measurement with a sinusoidal input at frequency kf_f for $k = 1, 2, \ldots, 10$. For example, the case when $J = 5$ is shown in Fig. 3. This relationship is approximate because it ignores super- and subharmonics in the jet velocity associated with the input frequency kf_f. Nevertheless, it is useful for determining a suitable initial input $\boldsymbol{a}_0$ by treating the system as linear; $\boldsymbol{a}_0$ is computed so that the input sinusoids, when modified by the frequency response, produce the output sinusoids with amplitudes given by $\bar{\boldsymbol{d}}$. With the input so determined, the corresponding periodic jet velocity is given by $\boldsymbol{d}_0$, and in general $\boldsymbol{d}_0 \neq \bar{\boldsymbol{d}}$; thus, some adjustment of the input is required. The Jacobian $K(\boldsymbol{a}_0)$ is estimated, and the input perturbation δ_a is determined from

$$\bar{\boldsymbol{d}} - \boldsymbol{d}_0 = K(\boldsymbol{a}_0)\delta_a$$

Depending on the norm of δ_a relative to the norm of $\boldsymbol{a}_0$, a smaller "step" may be taken and then K evaluated at the new operating point. This process is iterated until convergence is achieved, typically requiring 13 iterations for the hot-wire output signal to be deemed close enough to the desired waveform. Further details on the nature of the perturbation matrix and the iterative process used to improve the waveform may be found in Shoji [30].

A sample comparison of temporal hot-wire output signals with and without control, as compared with the ideal waveform, is shown in Fig. 4 for $J = 5$ at two different duty cycles, where the signal shown represents the temporal mean-subtracted vertical jet velocity $u_j - U_j$ just above the jet exit. To accomplish matching of $u'_{j,\mathrm{rms}}$ when performing the acetone PLIF experiments, $u'_{j,\mathrm{rms}}$ was precisely set to be the desired value just before PLIF imaging by adjusting a gain imposed on all input frequency components; this gain ranged from 0.9 to 1.1. This narrow range of gain, being close to unity, did not appreciably alter the jet waveforms. At this point, the input coefficients were frozen and the hot wire removed from the crossflow so that the imaging experiments could be performed. In Fig. 4, the temporal jet velocity distributions based on the frequency response model were distorted compared to the desired jet velocity waveform, whereas with iterative adjustment of the input, there was a clean square-wave-like response of the jet for both forcing cases shown, with the ability to achieve the desired sharp temporal upsweep required for periodic vorticity generation as achieved in earlier feedforward control experiments [22,24,26], but with far greater efficiency and control authority. Further details on the adaptive feedback control may be found in separate studies [42,43].

III. Results

For sinusoidal excitation of the JICF [30], the control parameters available to alter transverse jet penetration, spread, and mixing consisted of the frequency f_f and amplitude (via $u'_{j,\mathrm{rms}}$) of jet axisymmetric excitation. For square-wave forcing, in addition to frequency and amplitude, time scales in the excitation associated with the temporal pulse width τ or duty cycle α may also be varied to alter temporal vorticity generation and jet mixing characteristics. The stroke ratio L/D is typically used to characterize a nondimensional temporal pulse width, as noted previously. The L/D expression for a fully modulated JICF in Eq. (2) does not capture the net introduction of pulsed fluid into the flowfield, despite the fact that it would include mean jet fluid contributing to the total jet impulse, as discussed and used in Davitian et al. [26]. The relation for the stroke ratio associated with the approximate net pulse of fluid in Eq. (3), using the peak-to-peak velocity amplitude, works reasonably well in estimating the stroke ratio [24,28], but a more accurate method accounting for the integration of the net velocity pulse over an actual pulse width is possible via measurements of u_j.

The peak-to-peak velocity amplitude of a temporal square pulse Δu_j as measured at the center of the jet exit can be evaluated between a local minimum point before the upsweep of the square pulse ($u_{\mathrm{min},1}$) and the first local maximum point within the same square pulse ($u_{\mathrm{max},1}$), producing $\Delta u_j = u_{\mathrm{max},1} - u_{\mathrm{min},1}$. But to reflect the imperfect nature of the square wave, especially when low-level ringing takes place before the pulse, as observed in Fig. 4, an "actual"

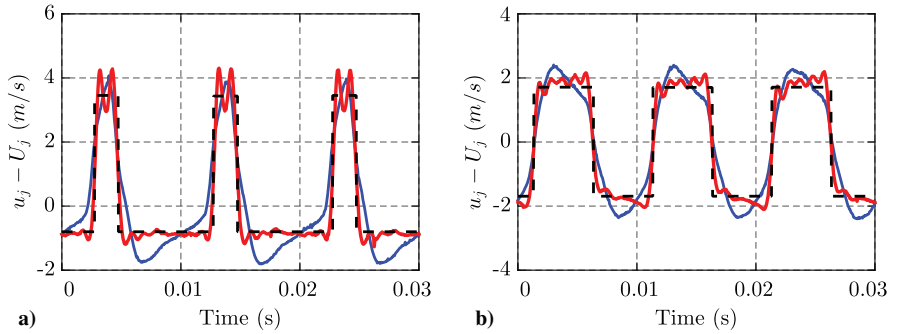

Fig. 4 Vertical velocity evolution measured at $(x, y, z = 0, 0, 0.2D)$ in response to excitation at $f_f = 100$ Hz, with matched $u'_{j,\mathrm{rms}} = 1.7$ m/s and input duty cycles a) $\alpha_{\mathrm{in}} = 20\%$ and b) 50%. Shown are the ideal square wave (dashed line), jet response without control (blue line) and jet response with control (red line).

velocity pulse is often defined via the "5% criterion" proposed by Johari et al. [20]. Here, 5% of Δu_j is added to the local minimum point $u_{\min,1}$ to define a so-called "5% point" in the temporal waveform, $u_{5\%}$. The actual (or "output") temporal pulse width τ_{out} is based on this quantity and is also different from the prescribed or input pulse width to the function generator, in that τ_{out} is defined as the time period between the 5% points on each side of the square pulse. Hence, both τ_{out} and $u_{5\%}$ may be applied when one integrates the effective velocity over time to produce the stroke ratio used in the present studies:

$$\left(\frac{L}{D}\right) = \frac{1}{D}\int_0^{\tau_{\text{out}}} (u_j - u_{5\%})\,\mathrm{d}t \tag{5}$$

In the present evaluation of stroke ratio, L/D was calculated for each square pulse over the entire set of temporal data sets for each condition, and then a mean stroke ratio was obtained by averaging at least 10 temporal cycles of square-wave forcing. For the alternative momentum flux ratios J explored here, a range of L/D values were studied, based on variable input duty cycles, forcing frequencies, and amplitudes. Stroke ratios extracted from Eq. (5) ranged from approximately 1.3 to 6.3, inclusive of the range of values explored previously [26] and which are relevant to optimal vortex ring formation [27]. Further details on comparing methods for determining stroke ratio may be found in Shoji [30]. Although the controlled and uncontrolled square waveforms differed from one another (e.g., as shown for $J = 5$ in Fig. 4), if one matches stroke ratio based on output temporal pulse width, the differences in the actual jet behavior were not significantly different, as discussed in Shoji [30], although the cleaner square waveform enabled more accurate control of these time scales.

A. Jet in Crossflow Structural Characteristics

The effects of square-wave excitation on JICF structural characteristics were explored for $J = 41$, 20, 10, and 5, the latter of which corresponded to an absolutely unstable USL when the jet was seeded with acetone [30]. Although many different square-wave excitation conditions were examined in this study, with excitation amplitudes in the range $1.0 \le u'_{j,\text{rms}} \le 3.0$ m/s [30], only a few of the most significant results will be documented here. These results focus on a matched value of the rms of the jet's vertical velocity perturbation $u'_{j,\text{rms}} = 1.7$ m/s, constituting approximately 26% of the mean jet velocity U_j at the exit plane, the same velocity perturbation explored in Davitian et al. [26]. A range of stroke ratios was examined with a fixed forcing frequency $f_f = 100$ Hz, as noted in Sec. II.B. As done for the sinusoidal excitation studies, instantaneous center-plane and mean cross-sectional acetone PLIF imaging was used to study jet structure and mixing properties. The effects of square-wave excitation at various L/D values were compared with one another and compared to sinusoidal excitation at the same frequency and value of $u'_{j,\text{rms}}$; note that, for sine wave excitation at 100 Hz, for all flow conditions, the USL was only marginally locked in, and the forcing was quite far from the natural frequency ranges f_o for the different J values, as documented in Shoji [30]. As noted previously, this lower forcing frequency enabled direct comparison with sinusoidal excitation at 100 Hz and a relatively large number of sinusoidal Fourier components to be used in creating the square wave. Separate studies of the effects of sinusoidal jet excitation and lock-in involved a JICF with a long PVC pipe connecting the nozzle and loudspeaker system [30] to eliminate swirl or other potential sources of jet asymmetry. The presence of this pipe did not alter the basic instability and structural characteristics of the JICF without forcing or with sine wave excitation. The pipe was removed for the present square-wave excitation experiments to enable the adaptive feedforward control to produce more accurate waveforms without internal resonance effects.

For the equidensity JICF with $J = 41$, where the USL was relatively weakly convectively unstable in the absence of excitation [7], square-wave forcing had the effect of increasing the jet spread and penetration over the unforced condition. In most cases, the degree of jet spread with square-wave forcing exceeded that with sinusoidal forcing, as shown via sample center-plane images in Figs. 5a–5d. But in some cases, there was relatively little alteration in the spread with square-wave forcing, and in none of the conditions explored ($1.29 \le L/D \le 6.32$, per Shoji [30]) were there distinct, periodic vortex rings formed in the center-plane jet structure. These observations were consistent with those by Davitian et al. [26] for relatively large J values. Interestingly, the mean cross-sectional images were generally made more symmetric with either square- or sine-wave forcing at this amplitude, as shown in Figs. 5e–5h, suggesting that mixing could be affected by such forcing, as will be discussed in Sec. III.B. Although mean cross-sectional images are shown here and in subsequent figures at only one downstream location ($x/D = 10.5$), as shown in Getsinger et al. [7] and Gevorkyan et al. [8], the cross-sectional shape was either asymmetric

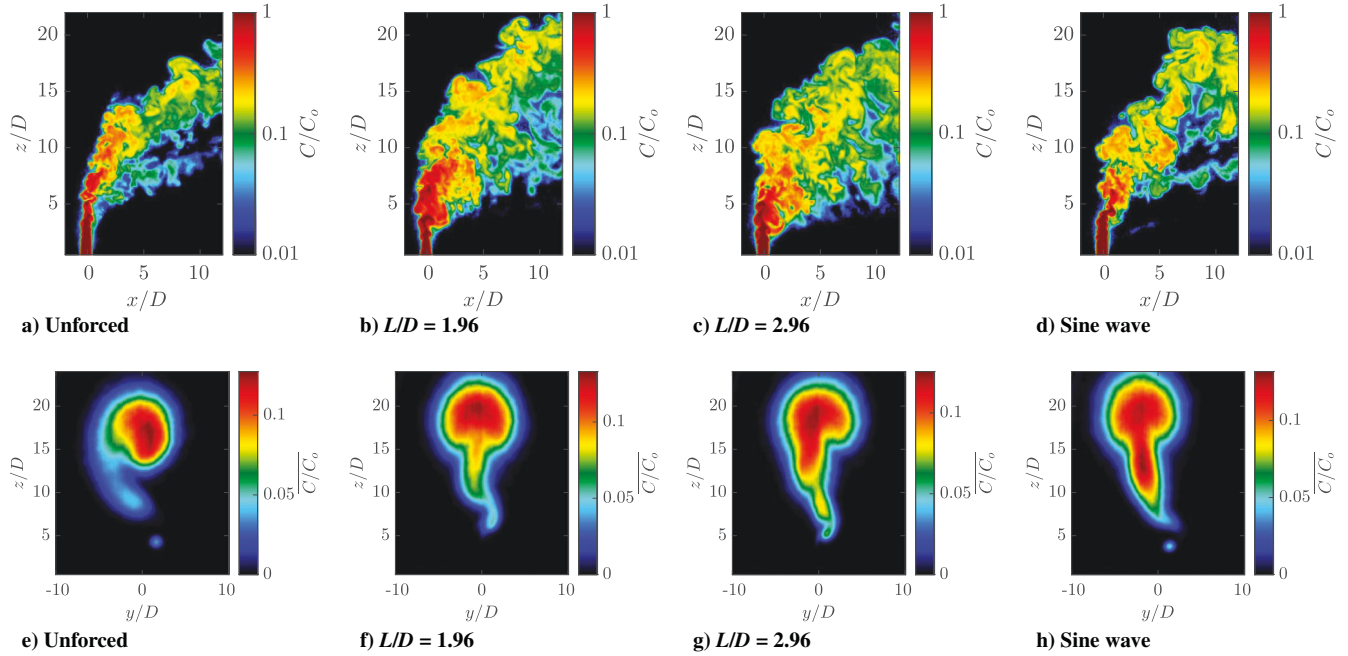

Fig. 5 a–d) Instantaneous center-plane images and e–h) corresponding mean cross-sectional images at $x/D = 10.5$ for the JICF at $J = 41$, for unforced and forced jet conditions.

or symmetric from the very beginning of the jet, and it evolves without altering its general orientation as one moves downstream.

As the momentum flux ratio was reduced by increasing U_∞, square-wave forcing became capable of creating periodically generated, more deeply penetrating vortex ring structures, as observed via smoke visualization in earlier studies [22,24,26]. Figure 6 shows instantaneous center-plane and mean cross-sectional far-field PLIF images for $J = 20$ under square-wave and sine-wave forcing, with matching values of $u'_{j,\mathrm{rms}} = 1.7$ m/s, contrasted with unforced jet behavior. Interestingly, the unforced JICF cross section's asymmetry for $J = 20$ (Fig. 6e) was opposite in its apparent orientation from that for $J = 41$ (Fig. 5e). This observation is previously documented to be a highly repeatable trend [7] for these two naturally convectively unstable shear-layer conditions. Based on linear stability analysis relevant to the JICF in this regime [44], these differences are likely the result of differences in naturally occurring helical growth rates in the jet's shear layer. Unlike the $J = 41$ case with square-wave excitation, deeply penetrating pufflike vortical flow structures started to be more clearly observed in Fig. 6, depending on stroke ratios L/D. An asterisk is indicated for stroke ratios L/D in Fig. 6 when periodic vortical structures were visually determined to be produced (e.g., $L/D = 2.81^*$ in Fig. 6c). In many cases (with additional ones shown in Shoji [30]), the vortical structures penetrate upstream, rather than vertically, in the lab reference frame. As L/D was systematically increased within the range 1.39 to 6.24 for a fixed $u'_{j,\mathrm{rms}} = 1.7$ m/s, there were specific instances in which particularly deeply penetrating puffs of fluid were produced (as shown in Shoji [30], corresponding to $L/D = 1.39$, 2.81, 3.15, 3.51, 3.82, and 4.20). But there were other cases for which these distinct vortical structures were not observed ($L/D = 1.91$, 2.15, 2.52, and 6.24). In general the range of stroke ratios producing maximal or "optimal" vortex penetration tended to be slightly lower here than the universal time scale for vortex ring formation, $L/D \approx 4$ [27]. But the present observations were generally consistent with conditions for maximum jet penetration observed for the transverse jet by Shapiro et al. [24] ($L/D \approx 1.7$–2.0 and 3.2–4.2) and Davitian et al. [26] ($L/D \approx 3.1$–3.7), despite the fact that the definition of stroke ratio is slightly different for these earlier studies. At larger stroke ratios associated with duty cycles approaching and exceeding 50% (e.g., for $L/D = 6.24$), center-plane flow structures differed little from those associated with sinusoidal excitation at the same value of $u'_{j,\mathrm{rms}}$. Despite the differences in instantaneous center-plane structure for different stroke ratios, the jets without deeply penetrating vortical structures altered the mean jet cross section just as significantly, though in different ways, as cases with deeply penetrating center-plane structures (e.g., Figs. 6f–6h).

As crossflow velocity increased further, reducing momentum flux ratio J to values approaching globally unstable USL conditions in the absence of forcing [7], square-wave excitation, especially at smaller stroke ratios, was able to create more deeply penetrating, periodic vortex rings. This trend is shown for the JICF at $J = 10$ in Fig. 7. The lowest stroke ratio ($L/D = 1.33$ in Fig. 7b) produced the most deeply penetrating vortical structures in the center plane. Remarkably, square-wave excitation for higher values of L/D approaching 4 (for example, $L/D = 3.41$) did not always produce such strong vortical structures and, in some cases, had a lesser degree of vortex penetration than did the JICF excited by sine-wave forcing (Fig. 7d). Mean cross-sectional structures similarly showed somewhat unexpected results; square-wave forcing conditions producing deeply penetrating vortical structures in the center plane in some cases produced relatively asymmetric cross sections (e.g., Fig. 7f) but, as expected, with evidence of a vertical trail of fluid associated with the vortex pulse. Larger stroke ratios producing lesser overall jet penetration were often associated with more symmetric cross-sectional structures (e.g., Fig. 7g). Overall, it appeared that the $J = 10$ JICF was somewhat less affected by or responsive to external forcing at $u'_{j,\mathrm{rms}} = 1.7$ m/s than the $J = 20$ case, most likely because of the strengthening natural instability in the upstream shear layer.

When the unforced JICF was produced with a low enough value of $J = 5$ to create a globally unstable upstream shear layer, strong square-wave forcing at lower stroke ratios, similar to cases for $J = 10$, was required to impact periodic vortex penetration. This is shown in Fig. 8. As for $J = 10$, conditions producing deeply penetrating vortical structures for $J = 5$ (for example, $L/D = 1.38$ and 2.10 in Figs. 8b and 8c) produced cross-sectional structures for which there was a remnant of the vertical vortex ring pulse (Figs. 8f–8g). Otherwise, as expected, the mean cross-sectional structures were relatively symmetric and CVP-like, consistent with existence and perturbation of an absolutely unstable shear layer.

B. Jet in Crossflow Mixing Characteristics

As in the case of the unforced JICF Gevorkyan et al. [8], mixing metrics used for the jet excited by axisymmetric square-wave forcing included quantities based on mean scalar field data and statistics

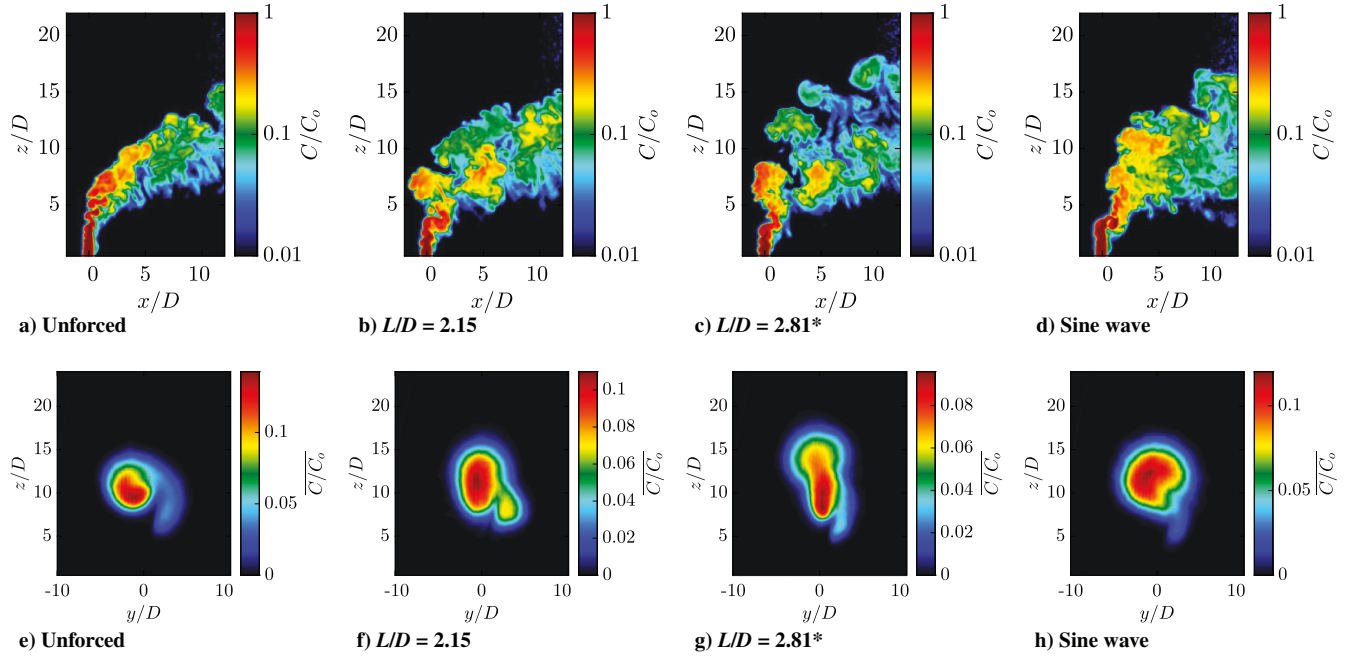

Fig. 6 a–d) Instantaneous center-plane images and e–h) corresponding mean cross-sectional images at $x/D = 10.5$ for the JICF at $J = 20$, for unforced and forced jet conditions. The stroke ratio with an asterisk corresponds to deeply penetrating vortical flow structures.

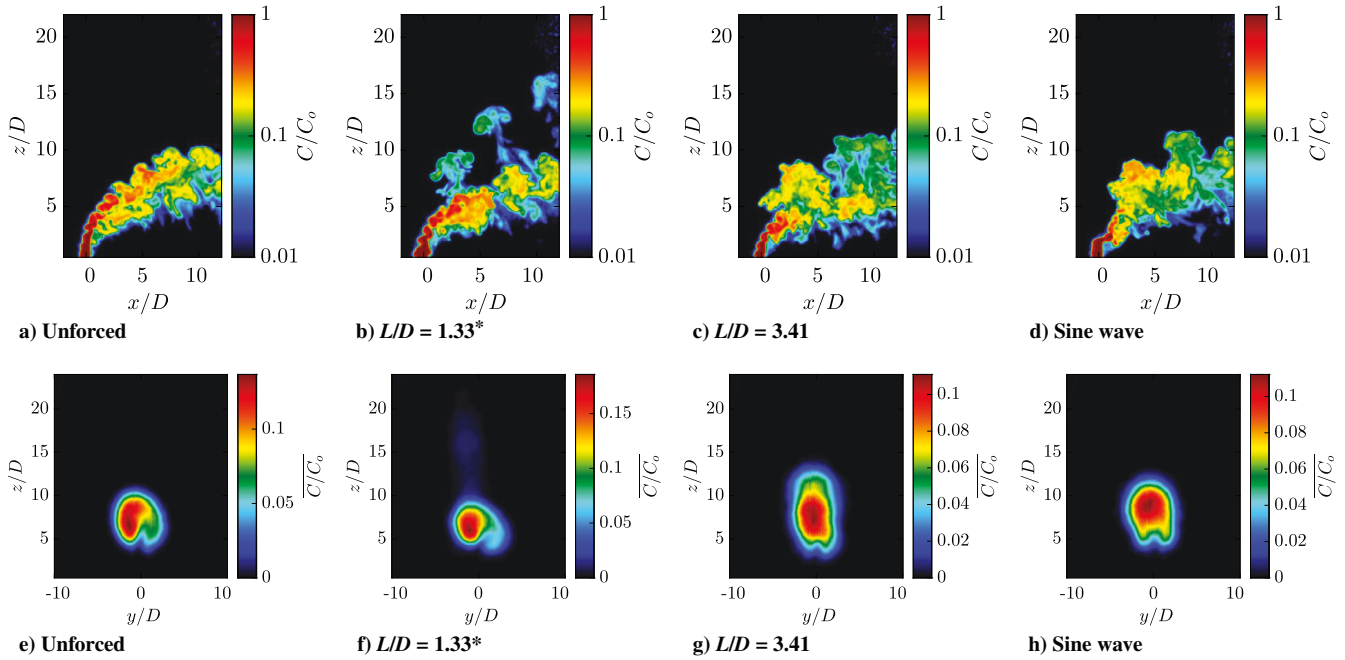

Fig. 7 a–d) Instantaneous center-plane images and e–h) corresponding mean cross-sectional images at $x/D = 10.5$ for the JICF at $J = 10$, for unforced and forced jet conditions. The stroke ratio with an asterisk corresponds to deeply penetrating vortical flow structures.

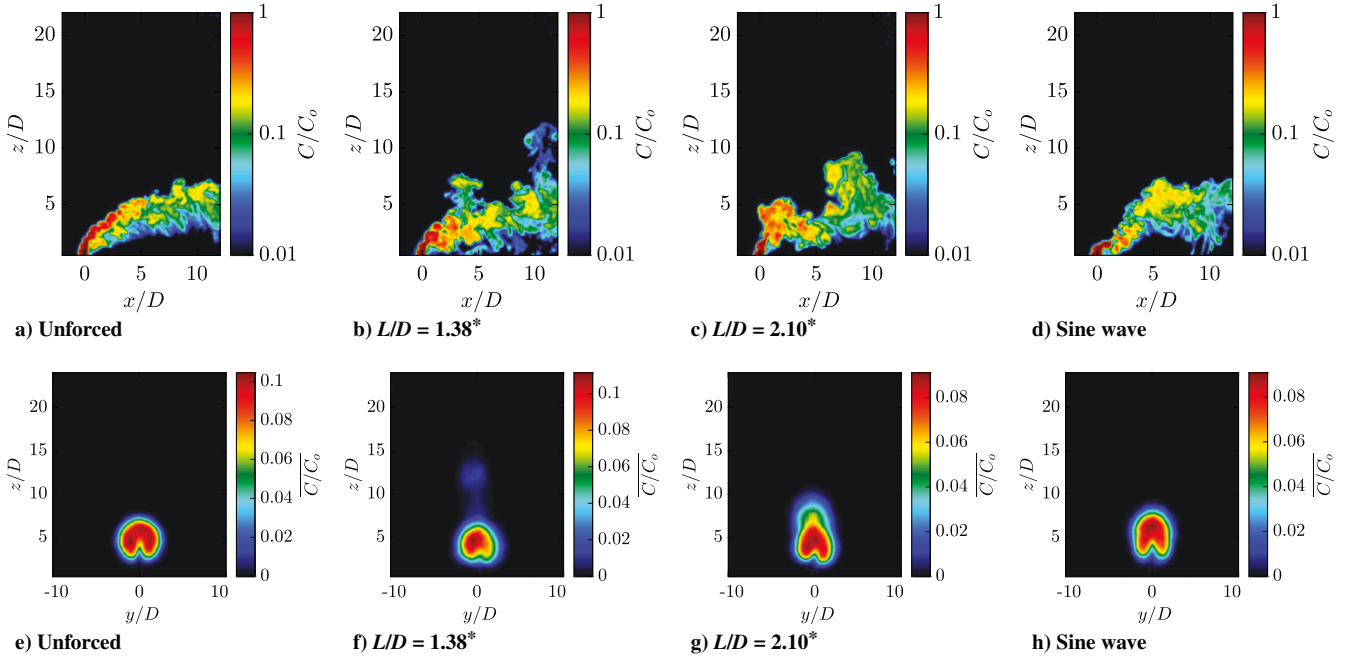

Fig. 8 a–d) Instantaneous center-plane images and e–h) corresponding mean cross-sectional images at $x/D = 10.5$ for the JICF at $J = 5$, for unforced and forced jet conditions. The stroke ratio with an asterisk corresponds to deeply penetrating vortical flow structures.

associated with instantaneous data. Mean mixing metrics specifically documented here include 1) jet penetration z_p (the z location of the top of the mean jet concentration as a function of downstream distance x), and 2) jet spread δ_n normal to each (forced) jet centerline trajectory in question. The jet centerline trajectory s_c was defined as that corresponding to the loci of maximum concentration in the mean images. Because external forcing for some forcing conditions yielded jet bifurcations, making jet trajectory determination more difficult to quantify, one could alternatively evaluate the jet spread and maximum concentration decay along the unforced jet centerline trajectory, for comparison. Scaling mixing metrics with respect to the unforced trajectory generally [30] showed the same trends as for scaling with the forced condition-specific mean jet trajectory s_c. For all mean mixing metrics, a threshold for the pixel intensity used to define the jet boundary was required; per the analysis in Gevorkyan [41] and Shoji [30], a minimum threshold value based on 1% of the maximum concentration in the mean center-plane images ($\bar{C}/C_o$) was employed. In most cases, the maximum concentration C_o corresponded to the concentration value inside the potential core region of the JICF, approximately unity. Additional mean metrics (e.g., the maximum mean concentration decay C_m/C_o), evaluated along the jet centerline trajectory, are documented in Shoji [30].

Molecular mixing in the forced JICF was quantified using the unmixedness parameter U, defined in Eq. (1), where a lower unmixedness corresponds to better local molecular mixing in a flowfield. We evaluated unmixedness here using both center-plane-based (x–z) and cross-section-based (y–z) laser sheet imaging. The center-plane-based unmixedness could be evaluated as a function of

alternative coordinates (x or s_c), and in the vertical and jet-normal directions, $U_{c,xz}$ and $U_{c,\mathrm{sn}}$, respectively, whereas the cross-section-based unmixedness U_{yz} was determined as a function of scaled downstream location x/D. As with the mean mixing metrics, results for unmixedness in the vertical (z) and forced jet-normal (s_c) orientations will be shown here. The center-plane-based unmixedness was quantified inside an interrogation area with a fixed seven-pixel width (in either x or s_c directions) at a given location in each instantaneous image. Although the width of this interrogation area was fixed, the length was varied so as to match the mean concentration within the area, $\bar{C}/C_o$ in Eq. (1), at all locations along the jet and for a range of flow and forcing conditions. This matching of mean concentrations in all interrogation areas and under all flow conditions enabled consistency in comparisons of instantaneous mixing metrics, as discussed in detail in Gevorkyan et al. [8]. In the cross-sectional view, the cross-section-based unmixedness was quantified at three different downstream locations $x/D = 2.5$, 5.5, and 10.5. The quantification of unmixedness was performed at all locations and in all instantaneous images using Eq. (1), and then mean unmixedness was determined by averaging over 500 instantaneous images at each location. Extensive analysis in Shoji [30] determined that statistical convergence for the mixing evaluation was satisfied with as few as 300 realizations. The complete set of data, plotted as a function of both downstream distance x/D and distance along the jet itself, relative to the unforced as well as the forced jet trajectory, is available in Shoji [30].

As indicated by the center-plane images in Fig. 5, square-wave excitation of the $J = 41$ JICF did produce increases in jet penetration and spread when compared with the unforced jet, with smaller improvements over sinusoidal excitation with a matched amplitude that was relatively high ($u'_{j,\mathrm{rms}} = 1.7$ m/s, relative to the mean jet velocity $U_j \approx 6.5$ m/s). This observation was borne out quantitatively, for example, in the variation in jet penetration shown in Fig. 9a for square-wave excitation in the range $1.29 \le L/D \le 6.24$. All excitation conditions produced improved jet penetration over the unforced case and, shown in Fig. 9b, improved normal jet spread as well. None of the square-wave excitation cases here produced periodic, deeply penetrating vortex "puffs", as seen for square-wave forcing at lower J values, and this was manifested in relatively similar effects of excitation on mixing metrics, especially the mean penetration as well as instantaneous molecular mixing metrics such as center-plane or cross-sectional unmixedness (Figs. 9c–9e). Mean jet spread did show differences among the various excitation conditions (e.g., in Fig. 9b). Interestingly, although sinusoidal excitation produced the least improvement in normal (and vertical) jet spread, it appeared to improve molecular mixing compared with square-wave forcing, although the differences were not significant. For $J = 41$, there were greater differences between local center-plane-based unmixedness at a given x location and that based on the cross-sectional jet slice (cf. Figs. 9d and 9e), and these were likely due to differences in the asymmetric/symmetric structure of the jet cross section, which were more difficult to capture appropriately in center-plane imaging. Improved cross-sectional symmetry over the unforced case via either square or sinusoidal excitation did appear to improve cross-sectional molecular mixing, as indicated in Fig. 9e. Cross-sectional symmetry and asymmetry could not be captured in the center-plane-based unmixedness metric, although the effects of jet spread were captured in the center-plane-based metric.

As J was decreased to 20, per the center-plane and cross-sectional imaging shown in Fig. 6, square-wave forcing had a greater influence on the creation of deeply penetrating vortical structures, and hence on jet structure and cross-sectional shape, than for $J = 41$. The effects of such forcing on mixing metrics for $J = 20$ are shown in Fig. 10. There were greater differences among the metrics for various square-wave conditions, with stroke ratios in the range $1.39 \le L/D \le 6.24$ and a fixed value of $u'_{j,\mathrm{rms}} = 1.7$ m/s. As expected, the conditions producing deeply penetrating vortex puffs also produced the greatest degree of penetration and spread, with the optimal conditions lying in the range $L/D \approx 3.15$–4.20. Interestingly, some deeply penetrating jet cases also appeared to create improved molecular mixing, especially in the range $2.81 \le L/D \le 3.15$, although the excitation conditions producing the best mixing did differ slightly depending on near- and far-field locations and depending on the coordinate against

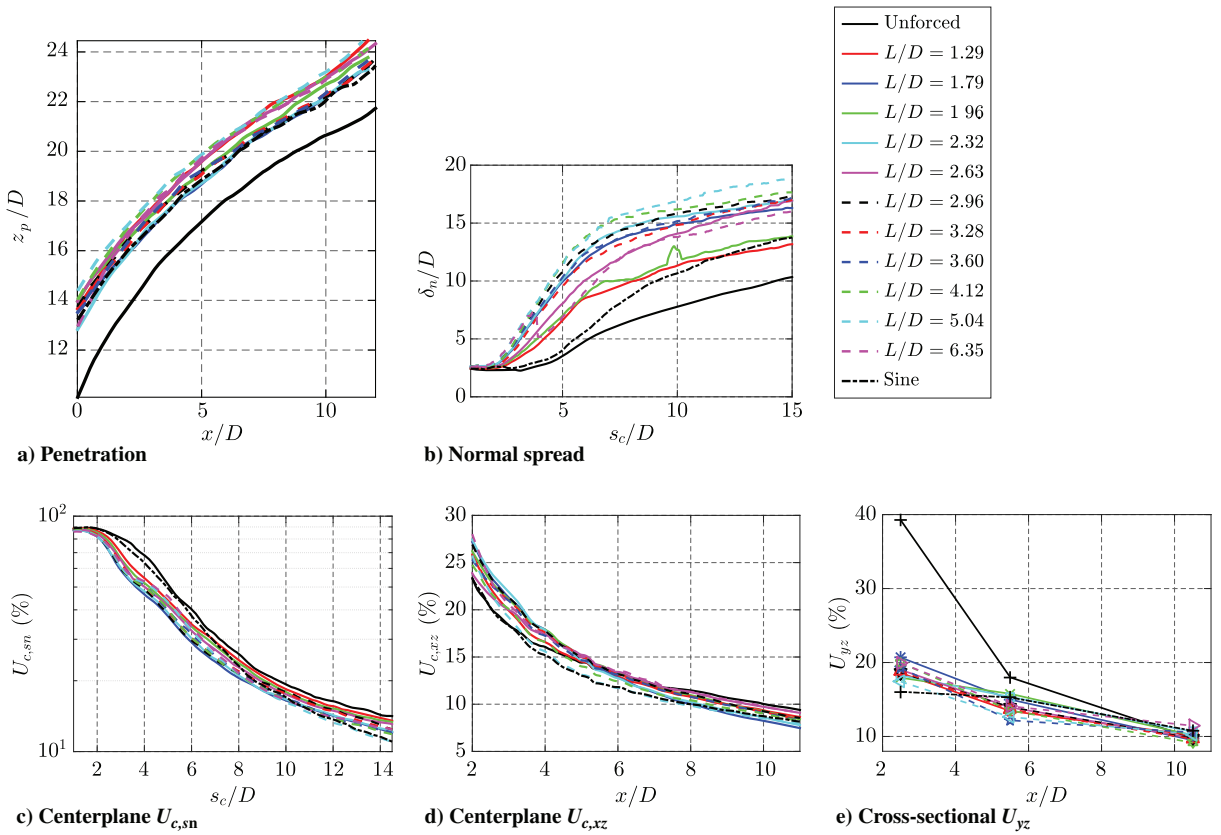

a) Penetration b) Normal spread

c) Centerplane $U_{c,\mathrm{sn}}$ d) Centerplane $U_{c,xz}$ e) Cross-sectional U_{yz}

Fig. 9 Various mixing metrics for the unforced and forced JICF at $J = 41$. None of the cases involves deeply penetrating vortical structures.

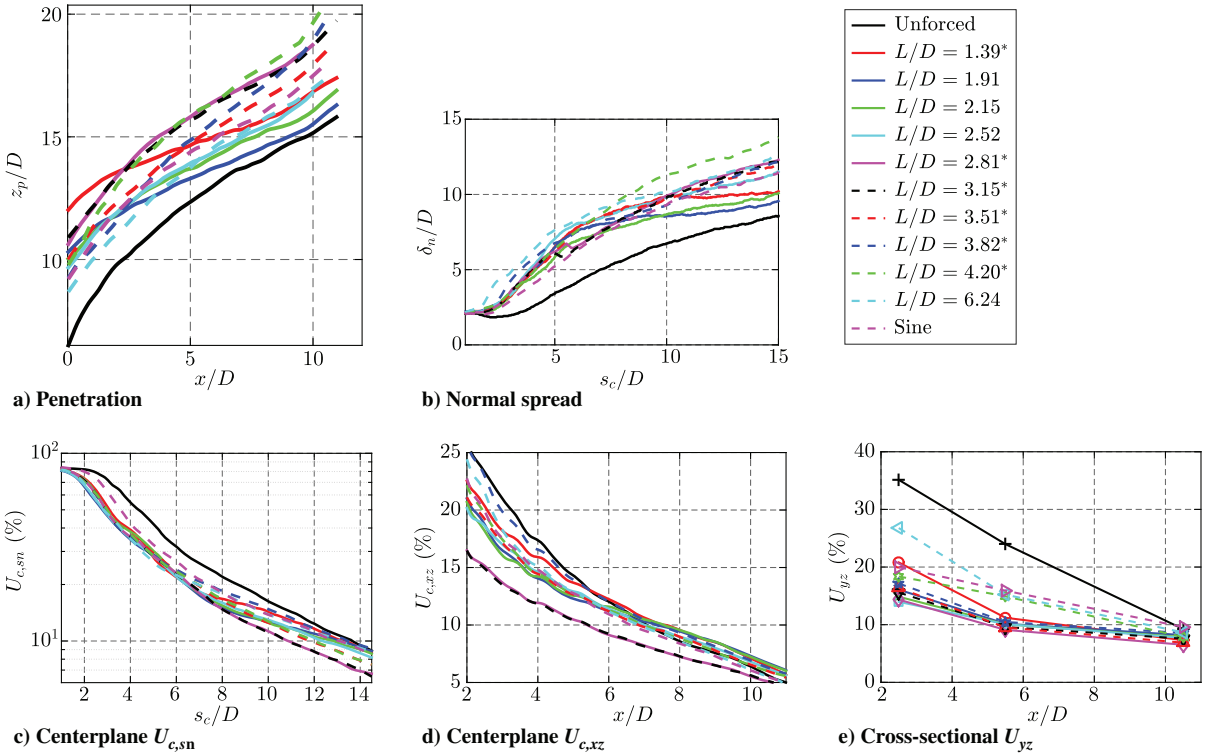

a) Penetration **b) Normal spread**

c) Centerplane $U_{c,sn}$ **d) Centerplane $U_{c,xz}$** **e) Cross-sectional U_{yz}**

Fig. 10 Various mixing metrics for the unforced and forced JICF at $J = 20$. Cases with an asterisk denote deeply penetrating vortical structures.

which unmixedness was plotted. At a very low stroke ratio producing deeply penetrating vortical structures ($L/D = 1.39$), near-field penetration was quite high, yet unmixedness tended not to be the lowest; hence, this condition was not typically deemed the best mixer. There were also general consistencies in trends between cross-sectional and center-plane-based unmixedness evaluated at a given downstream location x, and in most cases even similar quantitative values of unmixedness, with the exception of the unforced $J = 20$ case, one that was highly asymmetric in cross section. These results appeared to demonstrate that improved molecular mixing could be attained via improved cross-sectional symmetry as well as generation of periodic, deeply penetrating vortical structures, especially for stroke ratios L/D around 2.81–3.82. Overall, however, there was not a one-to-one correspondence among the greatest jet penetration and spread (Figs. 10a and 10b), the greatest improvement in cross-sectional symmetry (e.g., Figs. 6e–6h), and the greatest degree of molecular mixing (Figs. 10c–10e).

For the JICF with $J = 10$, which is closer to the critical momentum flux ratio $J_{cr} \approx 5$, per [30] for transition to a globally unstable USL, the effects of square-wave excitation on mixing in the range $1.33 \leq L/D \leq 6.16$ are shown in Fig. 11. All external forcing conditions shown here, including sinusoidal excitation, enhanced jet penetration

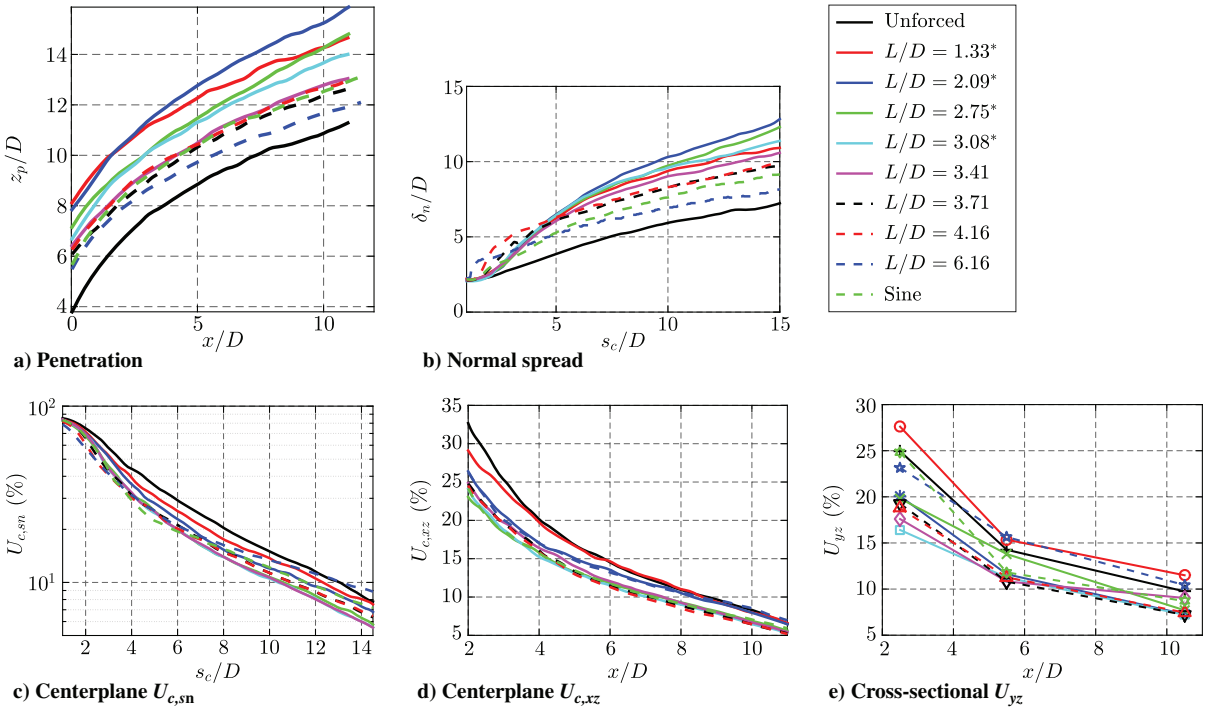

a) Penetration **b) Normal spread**

c) Centerplane $U_{c,sn}$ **d) Centerplane $U_{c,xz}$** **e) Cross-sectional U_{yz}**

Fig. 11 Various mixing metrics for the unforced and forced JICF at $J = 10$. Cases with an asterisk denote deeply penetrating vortical structures.

and spread as compared with the unforced case, similar to that observed for the $J = 20$ case. Consistent with the center-plane PLIF images (Fig. 7), square-wave forcing creating deeply penetrating vortical structures with stroke ratios in the range $1.33 \lesssim L/D \lesssim 3.08$ produced the greatest penetration and generally improved jet spread (Figs. 11a and 11b); this range for optimal penetration was lower than that for $J = 41$ ($L/D \approx 3.60$–5.04) and $J = 20$ ($L/D \approx 3.15$–4.20). On the other hand, quantification of molecular mixing via unmixedness in Figs. 11c–11e suggested that square-wave forcing with $L/D = 1.33$ and 2.09, which created the best jet penetration and spread, were among the poorest mixers (especially $L/D = 1.33$). Forcing conditions in which cross-sectional symmetry was improved but where deeply penetrating vortex rings were not necessarily created (e.g., for $L/D = 3.41$ as in Fig. 7c) did appear to create better molecular mixing. These results suggested that, especially for lower momentum flux ratio conditions such as $J = 10$, square-wave forcing creating deeply penetrating vortical structures may not necessarily produce improved molecular mixing. This observation resulted, at least in part, from the formation of a bifurcated jet structure for some cases with square-wave forcing; the actual mass exchange between jet and crossflow could be less vigorous even when the jet penetrated more extensively. For $J = 10$, overall optimal mixing tended to correspond to square-wave forcing in the range $L/D \approx 3.08$–4.16.

Finally, mixing characteristics were evaluated for $J = 5$, corresponding to the globally unstable USL in the absence of excitation; these metrics are shown in Fig. 12. Square-wave excitation conditions with the lowest values of L/D, 1.38, and 1.87, produced the deepest penetrating vortical structures in the center plane (e.g., Fig. 8b), and correspondingly maximum jet spread and penetration were observed for these conditions (see Figs. 12a and 12b); other excitation conditions produced somewhat lower penetration and spread yet with improvements over the unforced condition. The range of stroke ratios L/D for the best jet spread and penetration continued to be reduced as J was reduced from $J = 41$ to 5. Interestingly, for the instantaneous mixing metrics for $J = 5$ (Figs. 12c–12e), some square-wave forcing conditions that did not create deeply penetrating vortical structures produced the best degree of molecular mixing (e.g., $L/D = 3.04$, 2.72, and 2.45), in part resulting from a bifurcated jet's creating a lesser degree of mass exchange with the crossflow. But overall, square-wave forcing in the range $L/D \approx 2.45$–3.69 created optimal molecular mixing at $J = 5$ for a wide spatial region in the flow. As noted in Fig. 8, excitation for $J = 5$ did alter the cross-sectional shape for deeply penetrating jets, but it did not appear to alter the degree of cross-sectional symmetry itself, so that there was little correspondence between changes in symmetry and alterations in jet mixing, as shown in Figs. 8c–8e.

C. Optimal Vortex Penetration Versus Optimal Mixing

The trends in structure and mixing resulting from JICF square-wave excitation are interesting from many perspectives. Stroke ratios L/D producing deeply penetrating vortex structures, and thus maximum transverse jet mean penetration and spread, generally dropped off with a reduction in J. For $J = 41$, the maximum penetration and spread was attained for the range $L/D \approx 3.6$–5.0, whereas for $J = 20$, $L/D \approx 3.2$–4.2 tended to maximize penetration and spread; these values were close to the universal time scale for vortex ring formation, $L/D \approx 4$ per Gharib et al. [27]. At lower J values created by increasing crossflow velocity, the optimal stroke ratios continued to be reduced; for $J = 10$, optimal stroke ratios producing maximum vortex ring penetration lay in the range $L/D \approx 1.3$–3.1, whereas for $J = 5$, it was reduced to $L/D = 1.4$–2.1. These trends were consistent with those observed in JICF experiments by Davitian et al. [26] via smoke visualization.

These trends were also consistent with relevant computational studies of the evolution of vortex rings in crossflow [29] and the pulsed jet in crossflow with square-wave excitation [28]. These studies showed that optimal square-wave-like pulsing conditions creating the deepest-penetrating vortex structures in jets corresponded to values of L/D that decreased as crossflow velocity increased. The relationship was expressed in terms of the vortex ring velocity ratio $r_{\text{ring}} \equiv \Delta U_j/U_\infty$ and $L/D \approx \Delta U_j \tau/D$, so that, for a fixed velocity stroke ΔU_j, increasing the crossflow velocity U_∞ would cause the critical L/D value for maximum jet penetration to decrease. Sau and Mahesh [28] concluded that the optimal stroke ratio for the JICF converges to $L/D \approx 4$ as the crossflow velocity U_∞ approaches zero.

Trends documented in Sau and Mahesh [28], wherein increasing crossflow velocity for the pulsed JICF causes a reduction in the stroke ratio L/D, producing maximum jet/vortex penetration, may also be examined in the context of the present experiments. In addition to the data shown in Secs. III.A and III.B, experiments with other

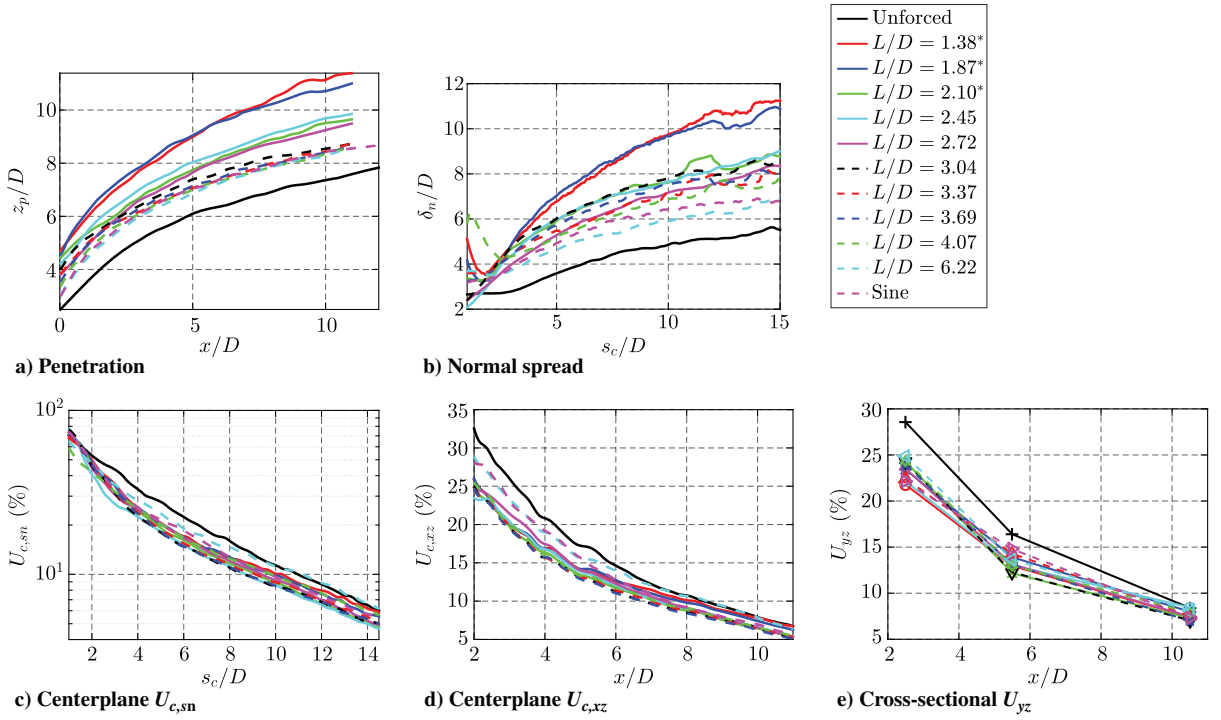

a) Penetration b) Normal spread c) Centerplane $U_{c,sn}$ d) Centerplane $U_{c,xz}$ e) Cross-sectional U_{yz}

Fig. 12 Various mixing metrics for the unforced and forced JICF at $J = 5$. Cases with an asterisk denote deeply penetrating vortical structures.

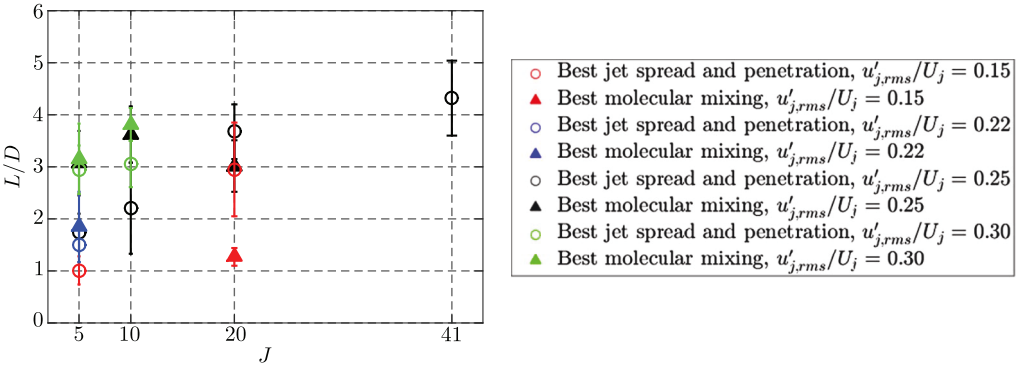

Fig. 13 Optimal range of stroke ratios L/D for varying J, estimated using Eq. (5) for the best jet spread and penetration (hollow circles) and molecular mixing (solid triangles).

forcing amplitudes were conducted and documented in Shoji [30]: $u'_{j,\mathrm{rms}} = 1.0$, 1.5, and 2.0 m/s, in addition to the excitation $u'_{j,\mathrm{rms}} = 1.7$ m/s. The range of stroke ratios producing the best jet spread and penetration, for various J values and for various forcing amplitudes, is shown by the hollow circles in Fig. 13. For a given forcing amplitude $u'_{j,\mathrm{rms}}$, there was a reduction in L/D producing maximum vortex penetration as U_∞ was increased and thus J reduced, consistent with the DNS of Sau and Mahesh [28]. In contrast, conditions producing optimal molecular mixing (lowest overall unmixedness) are shown by the solid triangles in Fig. 13. For example, as described earlier for square-wave forcing at $u'_{j,\mathrm{rms}} = 1.7$ m/s, the best molecular mixing was achieved roughly in the following ranges of stroke ratios: $L/D \approx 2.5$–3.5 for $J = 20$, $L/D \approx 3.1$–4.2 for $J = 10$, and $L/D \approx 2.5$–3.7 for $J = 5$. For $J = 41$, there were not significant differences in molecular mixing characteristics among the various excitation conditions. These values of L/D were generally in the same range as one another for various amplitudes $u'_{j,\mathrm{rms}}$, suggesting that stroke ratios producing the best molecular mixing were generally less independent on J. From a practical level, these results suggest that molecular mixing could be independently optimized, as compared with jet spread and penetration, depending on the application.

IV. Conclusions

These experimental studies document the effects of a range of temporal square-wave jet excitation conditions on transverse jet structure and molecular mixing characteristics. Examinations of equidensity gaseous jets in crossflow at a fixed jet Reynolds number ($Re_j = 1900$) and with momentum flux ratios relevant to a range of engineering applications ($5 \le J \le 41$) and for various forcing conditions revealed new insights into the control of such flows. For the first time, there was a quantification of trends in jet structure (degree of jet penetration, spread, bifurcation, and cross-sectional symmetry) as distinct from molecular mixing resulting from square-wave excitation. The nature of the unforced jet's upstream shear-layer instability, being either convectively or absolutely/globally unstable, also influenced the impact of square-wave excitation, suggesting that controlled, tailored excitation should depend on the jet's engineering application and flow regime.

Adaptive feedforward-controlled square-wave excitation enabled additional time scales associated with temporal pulse width τ_{out} to be used to alter jet in crossflow (JICF) structure and mixing. The nondimensional stroke ratio L/D, defined in terms of τ_{out} and mean jet velocity U_j via Eq. (5), was observed to have a significant effect on transverse jet structure when $u'_{j,\mathrm{rms}}$ was fixed among excitation conditions. For the JICF with a convectively unstable upstream shear layer (USL) in the absence of excitation ($J = 41$), square-wave and sinusoidal excitation at a relatively high amplitude ($u'_{j,\mathrm{rms}} = 1.7$ m/s) were observed to affect jet structure and cross section in fairly similar ways, causing the jet penetration to increase and the naturally asymmetric cross section to become more symmetric in the mean, yet not becoming quite counter-rotating vortex pair (CVP)-like (Fig. 5). There were no forcing conditions identified for which there were deeply penetrating, periodic vortex rings formed, and as a consequence, jet penetration and molecular mixing did not differ significantly among all excitation conditions for this case (Fig. 9). As crossflow velocity was increased and J was reduced, specific L/D ranges were observed for which periodic, deeply penetrating vortex ring formation did take place, and these L/D values tended to be reduced as J was reduced from $J = 20$ to 5. Conditions creating periodic, deeply penetrating vortex rings did not necessarily create symmetric, CVP-like cross-sectional structures, however (Fig. 7).

Penetration and spread (traditional mean metrics for jet mixing) only quantify the average boundaries for the jet in various ways. But molecular mixing is generally quantified based on instantaneous statistics, in our case via the unmixedness parameter [Eq. (1)], from which a more detailed exchange of mass between injectant and surroundings, at the molecular level, may be quantified. Hence, a bifurcated jet structure with large penetration may have relatively poor molecular mixing. But at moderate J values for which there was not an absolutely unstable USL without forcing, the cases with deeply penetrating vortex rings did, in some cases, improve molecular mixing as well as jet penetration. Strikingly, as J was reduced to $J = 5$, the low L/D stroke ratios producing deeply penetrating vortical structures and jets did not produce the optimal molecular mixing. The L/D ranges producing optimal molecular mixing tended to have little dependence on J, in fact, typically lying in the range $L/D \approx 3$–3.5. The cases for which molecular mixing was optimized (lowest unmixedness in both center-plane and cross-sectional views) tended to have symmetric cross sections, but not necessarily CVP-like, especially for the globally unstable JICF cases.

The variation in L/D values producing the greatest penetration and spread as well as (separately) improved molecular mixing, for different momentum flux ratios J, is summarized in Fig. 13. The reduction in the L/D values producing maximum vortex/jet penetration with lowered J was consistent with trends predicted in the simulations of Sau and Mahesh [28] as well as others' experiments [21,24]. But L/D values producing maximum jet penetration and spread did not always correspond to conditions with improved molecular mixing in either center-plane and cross-sectional views, in contrast to long-standing assumptions of the direct correlation of JICF penetration and molecular mixing [1,3]. Again, it was the improved symmetry in the jet cross section, as well as the CVP cross-sectional structure, that appeared to have the greatest effect on molecular mixing enhancement, and trends such as those documented in this study could be applied in a range of engineering applications for the transverse jet.

Acknowledgments

The authors thank Stephen Schein of UCLA for assistance during some of the data collection in these experiments. This project has been supported by the National Science Foundation (grant CBET-1437014), the U.S. Air Force Office of Scientific Research (grant FA9550-15-1-0261), and the Defense University Research Instrumentation Program (grant FA9550-10-1-0461).

References

[1] Margason, R. J., "Fifty Years of Jet in Cross Flow Research," AGARD, CP-534, Vol. 1, Neuilly sur Seine, France, 1993, pp. 1–141.

[2] Karagozian, A. R., "Transverse Jets and Their Control," *Progress in Energy and Combustion Science*, Vol. 36, No. 5, 2010, pp. 531–553. doi:10.1016/j.pecs.2010.01.001

[3] Kamotani, Y., and Greber, I., "Experiments on a Turbulent Jet in a Cross Flow," *AIAA Journal*, Vol. 10, No. 11, 1972, pp. 1425–1429. doi:10.2514/3.50386

[4] Fric, T. F., and Roshko, A., "Vortical Structure in the Wake of a Transverse Jet," *Journal of Fluid Mechanics*, Vol. 279, Nov. 1994, pp. 1–47. doi:10.1017/S0022112094003800

[5] Kelso, R. M., Lim, T. T., and Perry, A. E., "An Experimental Study of Round Jets in Cross-Flow," *Journal of Fluid Mechanics*, Vol. 306, Jan. 1996, pp. 111–144. doi:10.1017/S0022112096001255

[6] Cortelezzi, L., and Karagozian, A. R., "On the Formation of the Counter-Rotating Vortex Pair in Transverse Jets," *Journal of Fluid Mechanics*, Vol. 446, Nov. 2001, pp. 347–373. doi:10.1017/S0022112001005894

[7] Getsinger, D. R., Gevorkyan, L., Smith, O. I., and Karagozian, A. R., "Structural and Stability Characteristics of Jets in Crossflow," *Journal of Fluid Mechanics*, Vol. 760, Dec. 2014, pp. 342–367. doi:10.1017/jfm.2014.605

[8] Gevorkyan, L., Shoji, T., Getsinger, D. R., Smith, O. I., and Karagozian, A. R., "Transverse Jet Mixing Characteristics," *Journal of Fluid Mechanics*, Vol. 790, March 2016, pp. 237–274. doi:10.1017/jfm.2016.5

[9] Blanchard, J. N., Brunet, Y., and Merlen, A., "Influence of a Counter Rotating Vortex Pair on the Stability of a Jet in Crossflow: An Experimental Study by Flow Visualizations," *Experiments in Fluids*, Vol. 26, Nos. 1–2, 1999, pp. 63–74. doi:10.1007/s003480050265

[10] Camussi, R., Guj, G., and Stella, A., "Experimental Study of a Jet in a Crossflow at Very Low Reynolds Number," *Journal of Fluid Mechanics*, Vol. 454, March 2002, pp. 113–144. doi:10.1017/S0022112001007005

[11] Kelso, R. M., and Smits, A. J., "Horseshoe Vortex Systems Resulting from the Interaction Between a Laminar Boundary Layer and a Transverse Jet," *Physics of Fluids*, Vol. 7, No. 1, 1995, pp. 153–158. doi:10.1063/1.868736

[12] Karagozian, A. R., "An Analytical Model for the Vorticity Associated with a Transverse Jet," *AIAA Journal*, Vol. 24, No. 3, 1986, pp. 429–436. doi:10.2514/3.9285

[13] Megerian, S., Davitian, J., Alves, L. S. de B., and Karagozian, A. R., "Transverse-Jet Shear-Layer Instabilities. Part 1. Experimental Studies," *Journal of Fluid Mechanics*, Vol. 593, Dec. 2007, pp. 93–129. doi:10.1017/S0022112007008385

[14] Davitian, J., Getsinger, D., Hendrickson, C., and Karagozian, A. R., "Transition to Global Instability in Transverse-Jet Shear Layers," *Journal of Fluid Mechanics*, Vol. 661, Oct. 2010, pp. 294–315. doi:10.1017/S0022112010003046

[15] Getsinger, D. R., Hendrickson, C., and Karagozian, A. R., "Shear Layer Instabilities in Low-Density Transverse Jets," *Experiments of Fluids*, Vol. 53, No. 3, 2012, pp. 783–801. doi:10.1007/s00348-012-1329-x

[16] Gevorkyan, L., Shoji, T., Peng, W. Y., and Karagozian, A. R., "Influence of the Velocity Field on Scalar Transport in Gaseous Transverse Jets," *Journal of Fluid Mechanics*, Vol. 834, Jan. 2018, pp. 173–219. doi:10.1017/jfm.2017.621

[17] Chomaz, J.-M., "Global Instabilities in Spatially Developing Flows: Non-Normality and Nonlinearity," *Annual Review of Fluid Mechanics*, Vol. 37, 2005, pp. 357–392. doi:10.1146/annurev.fluid.37.061903.175810

[18] Iyer, P. S., and Mahesh, K., "A Numerical Study of Shear Layer Characteristics of Low-Speed Transverse Jets," *Journal of Fluid Mechanics*, Vol. 790, March 2016, pp. 275–307. doi:10.1017/jfm.2016.7

[19] Danckwerts, P. V., "The Definition and Measurement of Some Characteristics of Mixtures," *Applied Science Research*, Vol. A3, No. 4, 1952, pp. 279–296. doi:10.1007/BF03184936

[20] Johari, H., Pacheco-Tougas, M., and Hermanson, J. C., "Penetration and Mixing of Fully Modulated Turbulent Jets in Crossflow," *AIAA Journal*, Vol. 37, No. 7, 1999, pp. 842–850. doi:10.2514/2.7532

[21] Eroglu, A., and Breidenthal, R. E., "Structure, Penetration, and Mixing of Pulsed Jets in Crossflow," *AIAA Journal*, Vol. 39, No. 3, 2001, pp. 417–423. doi:10.2514/2.1351

[22] M'Closkey, R. T., King, J., Cortelezzi, L., and Karagozian, A. R., "The Actively Controlled Jet in Crossflow," *Journal of Fluid Mechanics*, Vol. 452, Feb. 2002, pp. 325–335. doi:10.1017/s0022112001006589

[23] Narayanan, S., Barooah, P., and Cohen, J. M., "Dynamics and Control of an Isolated Jet in Crossflow," *AIAA Journal*, Vol. 41, No. 12, 2003, pp. 2316–2330. doi:10.2514/2.6847

[24] Shapiro, S., King, J., M'Closkey, R. T., and Karagozian, A. R., "Optimization of Controlled Jets in Crossflow," *AIAA Journal*, Vol. 44, No. 6, 2006, pp. 1292–1298. doi:10.2514/1.19457

[25] Johari, H., "Scaling of Fully Pulsed Jets in Crossflow," *AIAA Journal*, Vol. 44, No. 11, 2006, pp. 2719–2725. doi:10.2514/1.18929

[26] Davitian, J., Hendrickson, C., Getsinger, D., M'Closkey, R. T., and Karagozian, A. R., "Strategic Control of Transverse Jet Shear Layer Instabilities," *AIAA Journal*, Vol. 48, No. 9, 2010, pp. 2145–2156. doi:10.2514/1.J050336

[27] Gharib, M., Rambod, E., and Shariff, K., "A Universal Time Scale for Vortex Ring Formation," *Journal of Fluid Mechanics*, Vol. 360, April 1998, pp. 121–140. doi:10.1017/S0022112097008410

[28] Sau, R., and Mahesh, K., "Optimization of Pulsed Jets in Crossflow," *Journal of Fluid Mechanics*, Vol. 653, June 2010, pp. 365–390. doi:10.1017/S0022112010000388

[29] Sau, R., and Mahesh, K., "Dynamics and Mixing of Vortex Rings in Crossflow," *Journal of Fluid Mechanics*, Vol. 604, June 2008, pp. 389–409. doi:10.1017/S0022112008001328

[30] Shoji, T., "Mixing and Structural Characteristics of Unforced and Forced Jets in Crossflow," Ph.D. Thesis, Univ. of California, Los Angeles, 2017.

[31] Huerre, P., and Monkewitz, P. A., "Local and Global Instabilities in Spatially Developing Flows," *Annual Review of Fluid Mechanics*, Vol. 22, No. 1, 1990, pp. 473–537. doi:10.1146/annurev.fl.22.010190.002353

[32] Barlow, J. B., Jr., Rae, W. H., and Pope, A., *Low-Speed Wind Tunnel Testing*, Wiley-Interscience, New Jersey, 1999.

[33] Poling, B. E., Prausnitz, J. M., and O'Connell, J. P., *The Properties of Gases and Liquids*, 5th ed., McGraw–Hill, New York, 2001.

[34] Hendrickson, C. S., "Identification and Control of the Jet in Crossflow," Ph.D. Thesis, Univ. of California, Los Angeles, Los Angeles, 2012.

[35] Lozano, A., Yip, B., and Hanson, R. K., "Acetone: A Tracer for Concentration Measurements in Gaseous Flows by Planar Laser-Induced Fluorescence," *Experiments in Fluids*, Vol. 13, No. 6, 1992, pp. 369–376. doi:10.1007/BF00223244

[36] Smith, S. H., and Mungal, M. G., "Mixing, Structure and Scaling of the Jet in Crossflow," *Journal of Fluid Mechanics*, Vol. 357, Feb. 1998, pp. 83–122. doi:10.1017/S0022112097007891

[37] Thurber, M. C., Grisch, F., Kirby, B. J., Votsmeier, M., and Hanson, R. K., "Measurements and Modeling of Acetone Laser-Induced Fluorescence with Implications for Temperature-Imaging Diagnostics," *Applied Optics*, Vol. 37, No. 21, 1998, pp. 4963–4978. doi:10.1364/AO.37.004963

[38] Su, L. K., and Mungal, M. G., "Simultaneous Measurements of Scalar and Velocity Field Evolution in Turbulent Crossflowing Jets," *Journal of Fluid Mechanics*, Vol. 513, Aug. 2004, pp. 1–45. doi:10.1017/S0022112004009401

[39] Clemens, N. T., "Flow Imaging," *Encyclopedia of Imaging Science and Technology*, edited by J. P. Hornank, Wiley, New Jersey, 2002, pp. 390–419. doi:10.1002/0471443395.img022

[40] Wang, G. H., and Clemens, N. T., "Effects of Imaging System Blur on Measurements of Flow Scalars and Scalar Gradients," *Experiments in Fluids*, Vol. 37, No. 2, 2004, pp. 194–205. doi:10.1007/s00348-004-0801-7

[41] Gevorkyan, L., "Structure and Mixing Characterization of Variable Density Transverse Jet Flows," Ph.D. Thesis, Univ. of California, Los Angeles, Los Angeles, 2015.

[42] Hendrickson, C., and M'Closkey, R., "Phase Compensation Strategies for Modulated-Demodulated Control with Application to Pulsed Jet

Injection," *ASME Journal of Dynamic Systems, Measurement, and Control*, Vol. 134, No. 011024, 2012, pp. 1–9.
doi:10.1115/1.4004768

[43] Hendrickson, C., and M'Closkey, R., "Compensation of Nonlinear Harmonic Coupling for Pulsed-Jet-Velocity Shaping," *AIAA Journal*, Vol. 51, No. 11, 2013, pp. 2600–2614.
doi:10.2514/1.J052241

[44] Alves, L. S. d. B., Kelly, R. E., and Karagozian, A. R., "Local Stability Analysis of an Inviscid Transverse Jet," *Journal of Fluid Mechanics*, Vol. 581, June 2007, pp. 401–418.
doi:10.1017/S0022112007005873

Y. Zhou
Associate Editor